Progress in Oceanography 241 (2026) 103647

Contents lists available at ScienceDirect

Progress in Oceanography

journal homepage: www.elsevier.com/locate/pocean

Internal tides in the Mediterranean Sea

Bethany McDonagh [a,b,*], Jin-Song von Storch [c,d], Emanuela Clementi [a], Nadia Pinardi [b]

[a] CMCC Foundation – Euro-Mediterranean Center on Climate Change, Italy
[b] Department of Physics and Astronomy, University of Bologna, Bologna, Italy
[c] Max Planck Institute for Meteorology, Hamburg, Germany
[d] Center for Earth System Research and Sustainability (CEN), University of Hamburg, Hamburg, Germany

ARTICLE INFO

Dataset link: https://doi.org/10.5281/zenodo.17949665

Keywords:
Ocean modelling
Internal waves
Internal tides
Mediterranean Sea
Ocean energy budget

ABSTRACT

The generation and propagation sites of internal tides in the Mediterranean Sea are mapped through a comprehensive high-resolution numerical study. Two ocean general circulation models are used for this: NEMO v3.6, and ICON-O, both hydrostatic ocean models based on primitive equations with Boussinesq approximation, where NEMO is a regional Mediterranean Sea model with an Atlantic box, and ICON a global model. Internal tides are widespread in the Mediterranean Sea. The primary generation sites: the Gibraltar Strait, Sicily Strait/Malta Bank, and Hellenic Arc, are mapped through analysis of the tidal barotropic to baroclinic energy conversion. Semidiurnal internal tides can propagate for hundreds of kilometres from these generation sites into the Algerian Sea, Tyrrhenian Sea, and Ionian Sea respectively. Diurnal internal tides remain trapped along the bathymetry, and are generated in the central Mediterranean Sea and southeastern coasts of the basin. The total energy used for internal tide generation in the Mediterranean Sea is 3.31 GW in NEMO and 1.52 GW in ICON. Wavelengths of the first baroclinic modes of the M2 tide are calculated in various regions of the Mediterranean Sea where internal tides propagate, comparing model outputs to a theory-based calculation. The models are also validated and intercompared to investigate the differences between them in their representation of internal tides.

1. Introduction

Internal, or baroclinic, tides are internal waves at tidal frequencies, which are generated when barotropic tides interact with topography in the ocean, often at shelf breaks (Baines, 1982; Kelly and Lermusiaux, 2016), ocean ridges (Merrifield et al., 2001; Niwa and Hibiya, 2001), and in narrow straits (Morozov et al., 2002; Buijsman et al., 2014). These waves can dissipate close to their generation sites in the case of high mode internal tides, or propagate away for up to thousands of kilometres, in the case of low-mode, superinertial waves (Arbic, 2022). Internal tides are responsible for around 1.0 TW of energy dissipation in the global ocean (Egbert and Ray, 2003; Morozov, 2018), meaning that understanding their sites of generation, propagation, and energy dissipation is of great importance when detailing the energy budget of the global ocean. Internal tides also contribute to deep ocean mixing (Munk and Wunsch, 1998), so they need to be correctly represented in numerical ocean general circulation models.

In many modern ocean general circulation models, the dissipation of energy from internal tides is represented with a parameterisation of tidal mixing, commonly that of St. Laurent et al. (2002). However, these parameterisations only represent a fraction of the total internal tidal energy dissipation, in particular that of high-mode internal tides which dissipate at their generation sites. The remaining energy, which relates to the low modes of superinertial internal tides, is propagated away and often missed by such parameterisations. Since the critical latitude for diurnal internal tides is 30°, in the Mediterranean Sea, due to its latitude range of 30°N–46°N, diurnal internal tides remain trapped along the bathymetry, while semidiurnal internal tides are supercritical and are able to freely propagate away from their generation sites, so both the dissipation of internal tidal kinetic energy close to the generation site and wave propagation over long distances need to be considered in the model's mixing parameterisations.

In most of the Mediterranean Sea, the amplitude of barotropic tides is lower than in many other regions of the global ocean, except at the Gibraltar Strait, Gulf of Gabes, and the North Adriatic Sea (Tsimplis et al., 1995; McDonagh et al., 2024). However, regional studies within the Mediterranean Sea such as Morozov et al. (2002), Oddo et al. (2023), and Alford et al. (2012) have indicated that strong internal tide generation occurs in several regions of the Mediterranean Sea, notwithstanding the low amplitude barotropic tidal energy. Additionally, these works suggest that a basin-wide study is needed, which is currently lacking in the literature.

* Corresponding author at: CMCC Foundation – Euro-Mediterranean Center on Climate Change, Italy.
E-mail address: bethany.mcdonagh@cmcc.it (B. McDonagh).

https://doi.org/10.1016/j.pocean.2025.103647
Received 25 November 2024; Received in revised form 28 November 2025; Accepted 8 December 2025
Available online 15 December 2025

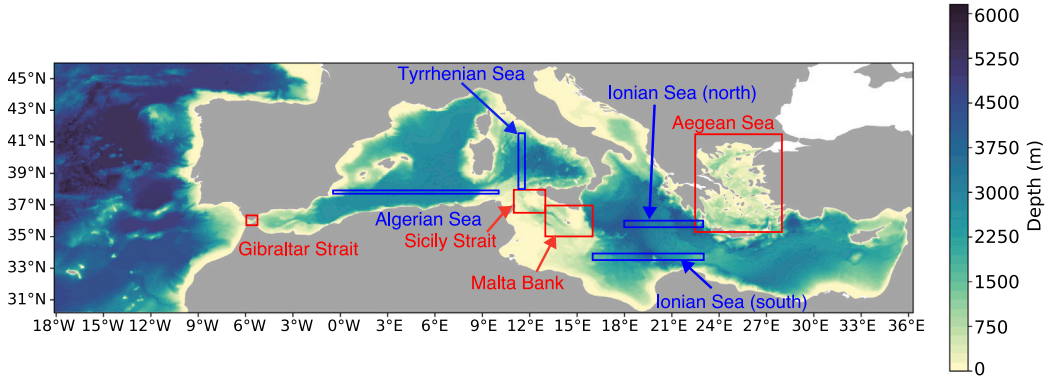

Fig. 1. Map of NEMO model domain with model bathymetry in coloured contours. Key regions from previous literature for internal tides studies are highlighted in red boxes, and further regions of study in this work are in blue boxes (see Section 4.3 and supplementary material).

The Gibraltar Strait is a region in which internal tides are studied in more detail, through both observational and modelling methods. Morozov et al. (2002) finds that semidiurnal vertical oscillations due to internal tide generation at the Camarinal Sill have amplitudes exceeding 200 m, and that this energy causes turbulent mixing in the Gibraltar Strait. Internal tides in the Gibraltar Strait contribute to the bottom pressure (Candela et al., 1990), and propagate in both directions from the Camarinal Sill (Lafuente et al., 2000).

Studies such as Gasparini et al. (2004) and Oddo et al. (2023) investigate internal tides in the central Mediterranean Sea, finding that internal tides are generated over the complex topography in both the Sicily Strait (Gasparini et al., 2004), and Malta Bank (Oddo et al., 2023), affecting the dynamics in both regions. The Messina Strait is another region of internal tide generation (Bignami and Salusti, 1990; Morozov, 2018), although many general circulation models, including those used in this study, do not resolve the Messina Strait, which is 3 km wide at the narrowest point. Other observational studies have been carried out in the Aegean Sea such as Alford et al. (2012), where Doppler current profiles are used to identify propagating semidiurnal internal tides, and in the Mid-Adriatic (Mihanović et al., 2009), where potential trapped diurnal internal waves around islands are found. These studies have shown that internal tides are generated at several sites in the Mediterranean Sea, but research has often been limited by spatial and temporal availability of observational data, which comes mostly from cruises, and limited-area models. The propagation of internal tides in the whole Mediterranean Sea has not previously been investigated. A summary of the previously studied regions of internal tides within the Mediterranean is shown in Fig. 1.

In other regions of the ocean, and for the global ocean in its entirety, numerical studies prove to be valuable in understanding internal tides. Studies including Arbic (2022), Müller et al. (2012), Shriver et al. (2012), and Li et al. (2015, 2017) demonstrate the value of using a high-resolution general circulation ocean model to investigate internal tides in the global ocean. This is done through identifying the characteristics of the internal tides and diagnosing the generation and propagation of internal tides. Additionally, analysis of internal tide wavelengths and vertical structure modes are used to understand the limitations of the numerical models. Basin- wide studies of oceans and seas such as Niwa and Hibiya (2001) in the Pacific Ocean, and Kelly and Lermusiaux (2016) in the Atlantic Ocean show the crucial role of topography in the generation of internal tides. These investigations demonstrate how this phenomenon integrates into the larger framework of internal tidal energy dynamics, including its interactions with major ocean currents like the Gulf Stream. Internal tides also interact with mesoscale eddies, as discussed in Dunphy and Lamb (2014) and Guo et al. (2023), where eddies change the phase speeds and cause refraction of internal tides.

In this study, we carry out an analysis of numerical simulations to understand the dynamics of internal tides in the Mediterranean Sea, with particular emphasis on finding generation sites, regions of semidiurnal internal tidal propagation, and the vertical modes of internal tides. Two ocean general circulation models are used, each with hourly outputs over a one-month period. Section 2 details the modelling framework and the spectral analysis used throughout the work, in Section 3 the models are validated and intercompared, Section 4 contains results and discussion from the model outputs, and Section 5 provides a conclusion. Further details on the spectral analysis are available in Appendix A while more information on the Sturm–Liouville eigenvalue problem is in Appendix B. Supplementary results are in Appendix C and results for additional regions are in the supplementary material.

Table 1
Tidal constituent components forced in the NEMO model used for this work, with their respective periods and astronomical descriptions.

Tidal component	Period (hours)	Description
M2	12.421	Principal lunar semidiurnal tidal constituent
S2	12.000	Principal solar semidiurnal tidal constituent
K1	23.934	Lunisolar diurnal tidal constituent
N2	12.658	Larger lunar elliptic semidiurnal tidal constituent
P1	24.066	Solar diurnal tidal constituent
Q1	26.868	Larger lunar elliptic diurnal tidal constituent
K2	11.967	Lunisolar semidiurnal tidal constituent

2. Model configurations

2.1. NEMO

The implementation of version 3.6 of the general circulation ocean model NEMO (Madec et al., 1998) in the Mediterranean Sea is used, based on the operational models described in Clementi et al. (2021) and Coppini et al. (2023); the NEMO model domain is shown in Fig. 1. This NEMO configuration has a horizontal resolution of $\frac{1}{24}^\circ$, and 141 uneven z* vertical layers with partial steps at the bottom. Lateral open boundary conditions are used in the Atlantic Ocean, coming from the Copernicus Marine Service global forecast and analysis (Galloudec et al., 2022), and in the Dardanelles Strait from a Marmara Sea box model (Maderich et al., 2015).

The Atlantic Ocean boundary includes tidal components and equilibrium tidal forcing is imposed as a surface forcing with eight tidal components (M2, S2, K1, O1, N2, Q1, K2, P1) from TPXO9 (Egbert and Erofeeva, 2002), which are described in Table 1.

Table 2
Comparison of some key features of the NEMO and ICON implementations used in this work.

Model component	NEMO	ICON
Region	Mediterranean Sea with Atlantic Box	Global
Grid	Rectangular latitude-longitude	Icosahedral
Horizontal resolution	$\frac{1}{24}^\circ$ (3.8 km)	R2B9 (around 5 km)
Vertical resolution	141 z* levels with partial cells	128 z* levels without partial cells
Time step	120 s (baroclinic), 2 s (barotropic)	s
Tides	8 tidal equilibrium tidal forcing components (M2, S2, K1, O1, N2, Q1, K2, P1) in the momentum and at the Atlantic lateral boundary	Full lunisolar tidal potential
Secondary tidal processes	None	Topographic wave drag and self attraction and loading
Rivers	39 rivers from climatology	4 Mediterranean rivers from climatology
Bathymetry	GEBCO (30")	SRTM30 (30")
Vertical mixing scheme	TKE	TKE
Lateral diffusivity coefficient	1.2×10^8 m^2s^{-1}	0 (switched off)
Lateral viscosity coefficient	2.0×10^8 m^4s^{-1}	2.7×10^{-2} m^2s^{-1}, scaled with the grid size to the fourth power
Time step	120 s	120 s

The atmospheric forcing for the one-month period in 2022 analysed in this work starts from the six-hourly temporal resolution European Centre for Medium-Range Weather Forecasts (ECMWF) analyses for surface atmospheric variables, which are used by bulk formulae from Pettenuzzo et al. (2010) to calculate water, momentum, and heat fluxes. Furthermore, monthly mean climatologies for the 39 rivers in the Mediterranean Sea with the largest water flux are included at the surface layer. These are from Fakete et al. (1999) for the Ebro, Nile, Po, and Rhône rivers, Raicich (1996) for the Vjosë and Seman rivers, Demiraj et al. (1996) for the Buna and Bojana rivers, and Deliverable of Perseus (2012) for the remaining 32 rivers. Initial conditions of temperature and salinity are from the 2005–2012 winter climatology of Boyer et al. (2013), and the model was integrated from January 2015, so has an extensive spin-up period.

The model bathymetry is provided by GEBCO Bathymetric Compilation Group 2014 (2014) at 30-arc-second resolution, bilinearly interpolated onto the model grid, with some additional changes in several locations. Firstly, two points in the Bay of Biscay are closed and several points along the Croatian coastline are modified for stability purposes, to avoid spurious tidal generation around complex bathymetry. These modifications follow Clementi et al. (2021). Furthermore, several points in the Gibraltar Strait are modified to improve the mass transport values and avoid spurious vertical mixing in the Gibraltar Strait region. These changes are made according to McDonagh (2024). Vertical mixing in the model configuration uses a turbulent kinetic energy (TKE) closure scheme, which is again tuned following McDonagh (2024).

2.2. ICON-O

To provide a robust numerical analysis of internal tides in the Mediterranean Sea, a second dataset, derived from a global scale implementation of the ICON-O (Korn et al., 2022) primitive equations general circulation model, is used.

ICON-O uses an icosahedral grid, which splits the Earth's surface initially into twenty equilateral triangles and then bisects these triangles further for higher resolution simulations, resulting in so- called R2B*n* resolutions, where *n* is the number of times that the original icosahedron is bisected (Giorgetta et al., 2018). The simulation of ICON-O used in this work has a resolution of R2B9, meaning that the initial grid is divided nine further times, which is approximately equivalent to a horizontal resolution of 5 km when interpolated onto a regular latitude-longitude grid. This resolution is slightly lower than, but comparable to, NEMO's $\frac{1}{24}^\circ$ horizontal resolution in the Mediterranean Sea. ICON-O has 128 z* vertical levels without partial cells at the bottom, and uses the SRTM30 bathymetry (Becker et al., 2009) interpolated onto the model grid. Narrow straits (Gibraltar, Dardanelles, and Bosphorus in the Mediterranean/Black Sea region) are manually checked to ensure that they are open, but no further modifications are made. The Black and Marmara seas are included in the ICON-O model, so no boundary condition is required at the Dardanelles Strait.

The world's fifty largest rivers are included in the configuration (Gates et al., 1993), including four that flow into the Mediterranean Sea: the Ebro, Nile, Po, and Rhône. These use flux values from the daily climatology by Röske (2006). Atmospheric forcing is from ERA5 (Hersbach et al., 2023) with a temporal frequency of one hour, at a resolution of $\frac{1}{4}^\circ$, interpolated onto the model grid.

Tides are included in ICON-O via a lunisolar gravitational term in the momentum equation, which is the horizontal component of the difference between the gravitational forces of the Sun and Moon and the centrifugal force due to the rotation of the Earth (Logemann et al., 2021). Therefore ICON-O includes all tidal components. The accuracy of tides in ICON at lower resolutions (R2B6 to R2B8) is assessed in von Storch et al. (2023).

Vertical mixing in ICON uses a TKE scheme also based on Gaspar et al. (1990) and has a similar configuration to NEMO for this parameterisation. The model uses further parameterisations of secondary tidal processes: topographic wave drag, and self-attraction and loading, which are not included in the NEMO configuration. Some of the key differences between the two model configurations are summarised in Table 2.

One month (March 2022) of data is analysed for each model, with hourly outputs of three-dimensional currents, temperature, salinity, Brunt-Väisälä frequency, and two-dimensional sea surface height.

3. Model validation and intercomparison

Before the analysis of the internal tide generation and propagation, a validation and intercomparison of the models is shown, with a focus

on the dynamics which affect internal tides, namely the barotropic tides, the ocean's vertical profile, and the model bathymetry. The core parts of the models are already validated in Clementi et al. (2021) and Coppini et al. (2023) for the NEMO model configuration and von Storch et al. (2023) for ICON, so in this section we focus on the aforementioned processes which are most relevant to this work.

3.1. Barotropic tides

The tidal amplitudes and phases are calculated through a harmonic analysis of sea surface height and first compared to data from TPXO9 (Egbert and Ray, 2003). It should be noted that one month of data is a short time period for a robust validation and comparison with data from TPXO9 and tide gauges, but can still be useful for the purpose of model intercomparison. Amplitudes and phases of the principal semidiurnal and diurnal tidal components (M2 and K1), and the vector difference between each experiment and TPXO9, are shown in Figs. 2 and 3. This analysis compares the two models with data from TPXO9 bilinearly interpolated onto the model grid. For the analysed month, placements of the maximum amplitudes and amphidromic points are broadly similar in both the experiments within the Mediterranean Sea in the M2 component. However, it is clear that the models do not always correctly capture the tidal amplitude in some key locations for internal tide generation.

In the ICON implementation, the Alboran Sea and Sicily Strait regions have particularly large differences from TPXO9 for the M2 component (Fig. 2e.), and in the K1 component, the difference is largest in the western Mediterranean Sea. In the NEMO experiment, the overestimation of the K1 amplitude is limited to the north Adriatic Sea, where K1 is already typically large. The NEMO experiment represents the M2 component well, with underestimation of tidal amplitude limited to a few regions. The amphidromic points of the models and TPXO9 are similarly positioned in the M2 component (Fig. 2f. and g.), but are less coherent in K1 (Fig. 3f. and g.), where NEMO captures the Sicily Strait amphidromic point, but ICON does not, and both models are notably different from TPXO9 in the Eastern Mediterranean Sea, missing the phase contour lines in the western basin.

Another validation method for the barotropic tides in the Mediterranean Sea is to utilise the basin's array of tide gauges. This provides a strong source of truth compared to the TPXO9 model, but not all areas of the basin are well-covered by these datasets. Fig. 4 shows a map of the available tide gauges in the Mediterranean Sea in March 2022 and a bar chart where tidal amplitude and phase are compared to the array of tide gauges over the whole Mediterranean Sea. In general, NEMO has lower RMSEs at a basin scale, in most tidal components for both amplitude only and the amplitude-phase combination. The exception to this is the P1 component. In the two components of the most interest in this study, M2 and K1, NEMO outperforms ICON when comparing to tide gauge data.

3.2. Ocean vertical profiles

An important measure when analysing internal tides is the ocean stratification, given that it is expected that models with a more stratified ocean are more likely to produce stronger internal tides. The energy per unit volume in a propagating internal tide at the semidiurnal frequency, E_f according to Baines (1982) and Green et al. (2010), is:

$$E_f = 0.5\rho_0(u'^2 + w'^2 + N^2\eta^2) \quad (1)$$

where ρ_0 is the constant reference density, u' and w' are perturbation velocities in the horizontal and vertical directions respectively, N is the Brunt-Väisälä frequency, and η is the displacement of a streamline of the internal wave field, ψ, which is itself defined by $u_i = -\psi_z$, $w_i = -\psi_x$ (Baines, 1982).

However, since the Brunt-Väisälä frequency is calculated within the model time step, it is not comparable to the time-mean Brunt-Väisälä frequency from an observational dataset or climatology. Considering this, and given that the Brunt-Väisälä frequency profiles are based on equation of state formulae of temperature and salinity, here we show comparisons of the temperature and salinity profiles for the Mediterranean Sea in the models and two observational datasets. These datasets are the World Ocean Database (Mishonov et al., 2024) and CORA (Copernicus Marine Service, 2024). The World Ocean Database observations are interpolated onto a global 1/4° grid, and the data from March 2015–2022 is used, as it is the closest climatology to the time period of the model outputs. The CORA dataset is on a 1/2° grid, but has monthly outputs, so we use the data from March 2022. These datasets are bilinearly interpolated onto the model grids when bias and root mean square error are calculated. Following this, the squared Brunt-Väisälä frequency profiles of the two models are intercompared, both for the Mediterranean Sea and the regions defined in Fig. 1.

Fig. 5 shows the temperature and salinity profiles, biases and root mean square errors of the two models compared to the two observational datasets described above. The first 1500 m are shown since this is the depth limit of the WODB dataset. The salinity profiles (Fig. 5d.-f.) are very clear in that NEMO is far closer to both of the observational datasets than ICON. The largest RMSE of NEMO is at the surface when compared with the WODB dataset, and it does not exceed 0.3 PSU as a basin mean, with the bias tending towards zero at deeper levels. However, in ICON, a bias of −2 PSU is exceeded at the surface when compared to either observational dataset. It is clear that ICON underestimates the salinity in the Mediterranean Sea, potentially since it is not well-tuned for this high-salinity basin, unlike the NEMO configuration which was developed specifically for the Mediterranean Sea. The accuracy of the temperature profiles are dependent on the observational dataset used: ICON is closer to the WODB dataset while NEMO is closer to CORA, in terms of bias. The profiles are also depth-dependent, where the NEMO-WODB comparison has the highest RMSE of the four profiles in the first 500 m, overestimating temperature in the upper and intermediate layers, and has the lowest RMSE in the deeper layers. The RMSE of ICON, especially when compared to CORA, is more consistent throughout the profile. These differences are likely due to the relative strengths and weaknesses of the two selected observational datasets: the WODB uses eight years of March data, so it could miss any extremes that were specific to March 2022, while CORA has a lower resolution, so can fail to capture mesoscale features such as eddies that affect temperature in the upper layers and any deep water formation events that can change the profile, especially during winter months. Profiles of the squared Brunt-Väisälä frequency are shown in Appendix C.

3.3. Bathymetry

The generation of internal tides is sensitive to changes in bathymetry since internal tides are generated along the topography. The model bathymetry, as described in Table 2, comes from different sources in each experiment, and although they have the same resolution (30 arc-seconds), they are interpolated differently in each model due to the differing model grids. These bathymetry variations, although they are usually small, impact the generation regions of internal tides, and therefore their kinetic energy and direction of propagation. In most of the domain, the bathymetry is similar in both models, and a comparison of the entire basin is available in Appendix C. However, some of the differences in internal tide generation and propagation between the two models is connected to the different topography in some of the key internal tide generation regions, as is shown in Fig. 6. In the narrowest part of the Gibraltar Strait, the most important region in the Mediterranean Sea for internal tide generation, the bathymetry is deeper in the NEMO implementation than it is in that of ICON. This is likely to affect the generation of internal tides and their propagation throughout the western Mediterranean basin. Another key bathymetry difference is in the Malta Bank (Fig. 6h): in the ICON implementation

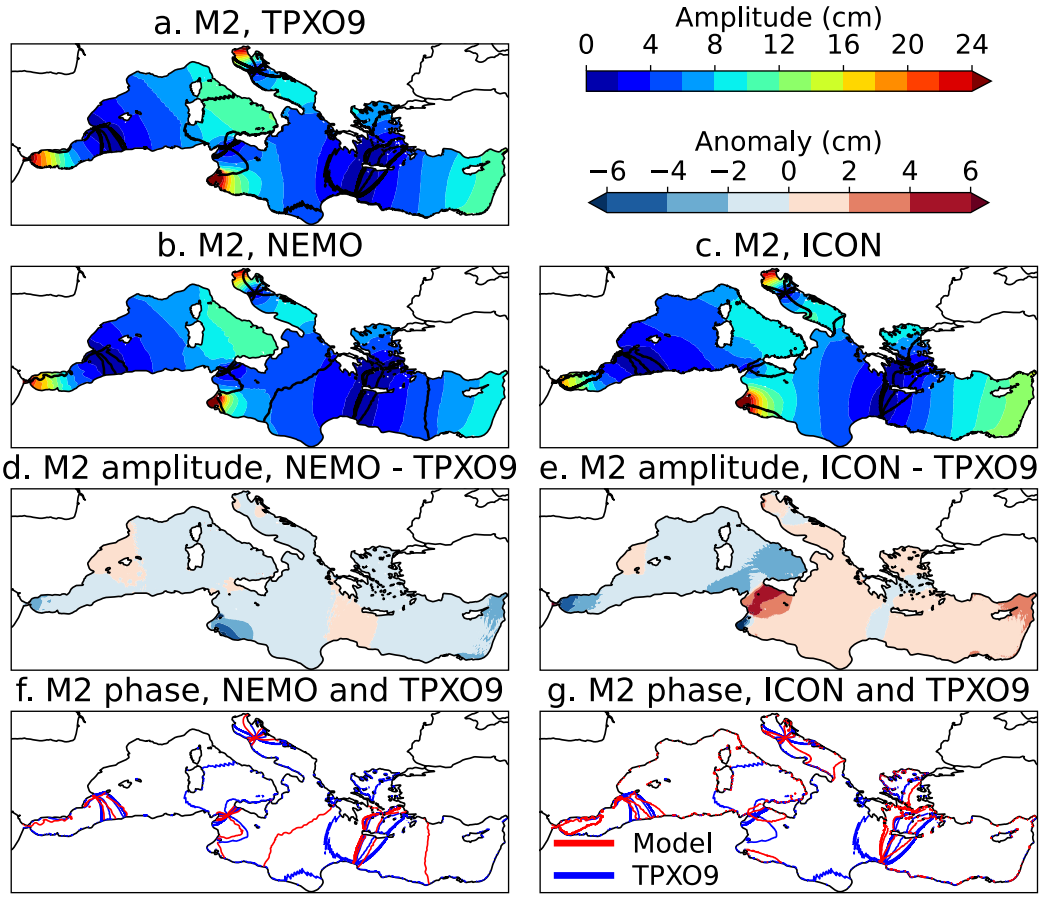

Fig. 2. Amplitude and phase of the M2 tidal component in a. TPXO9, b. NEMO, and c. ICON for March 2022, the amplitude difference between TPXO9 and d. NEMO and e. ICON, and the phase contours of TPXO9 compared to f. NEMO and g. ICON. The phase contours are 30° apart.

the bathymetry is steeper and placed differently in comparison to the NEMO experiment, and the Ionian Sea is deeper while the Sicily Strait passage is shallower in the ICON experiment compared to that of NEMO. Finally, the deeper Ionian Sea also affects the Hellenic Arc region (Fig. 6i).

4. Results and discussion

4.1. Internal tide generation

Internal tide generation can be quantified in terms of C, the conversion from barotropic tidal energy to internal tide energy (Kang and Fringer, 2012; Müller, 2013; Niwa and Hibiya, 2014; Li and von Storch, 2020), defined as:

$$C = \int_{-D}^{\eta} g\rho' W \, dz \tag{2}$$

where ρ' is the density perturbation associated with an internal tide, W is the tidal vertical velocity, η is the sea surface height, and D is the depth of the ocean. W is obtained from:

$$W(z) = -\nabla(D+z)U = U \cdot \nabla D + (D+z) \cdot \nabla U \tag{3}$$

where U is the barotropic horizontal tidal velocity, derived from a harmonic analysis of the horizontal currents, based on the method of Foreman et al. (2009).

To derive ρ' associated with an internal tide, the full density is decomposed into:

$$\rho(x,y,z,t) = \rho_0 + \rho_b(x,y,z) + \rho^*(x,y,z,t) \tag{4}$$

where ρ_0 is a constant reference density, and ρ_b is the background time-mean density at each grid point, so that $\rho_0 + \rho_b$ is the total background mean density. A harmonic analysis on the time-varying component, ρ^*, is carried out to obtain the density perturbation ρ' associated with internal tides at each tidal frequency.

Once C is calculated using the values of u, v, and ρ' for each of the eight tidal components included in the experiments, it is summed to find a total value for C. Positive values of C indicate the generation of internal tides by barotropic tides. Fig. 7 shows a map of C for the Mediterranean Sea in the two experiments. These maps confirm and quantify the generation sites of internal tides.

Barotropic to baroclinic energy conversion for internal tide generation takes place in a wide variety of regions, but most notably in the Gibraltar Strait/Alboran Sea, the Algerian Sea, the Tyrrhenian Sea, the Sicily Strait/Malta Bank, the Ionian Sea, and in NEMO, the eastern and north-western Mediterranean Sea in general. Looking at these regions more closely in Fig. 8, we can see that the narrow and steep Gibraltar Strait (Fig. 8a, d) is a major generator of baroclinic tidal energy, where tidal velocity is high. The Hellenic Arc (Fig. 8c, f) is the next most significant region for generation of internal wave kinetic energy, with large values of C particularly widespread in the NEMO experiment. The narrow passage in the Sicily Strait and the steep slope in the Malta Bank (Fig. 8b, e) also have large values of C. The higher values of C in NEMO in the Malta Bank come from the stronger baroclinic K1, as K1 is the predominant internal tide component in this region (Oddo et al., 2023). This is in combination with the modified bathymetry gradient of the Malta Bank in NEMO compared to ICON (Fig. 6h), which affects internal tide generation at this site. The region-averaged value of C in Fig. 1 regions is positive for both models with larger values

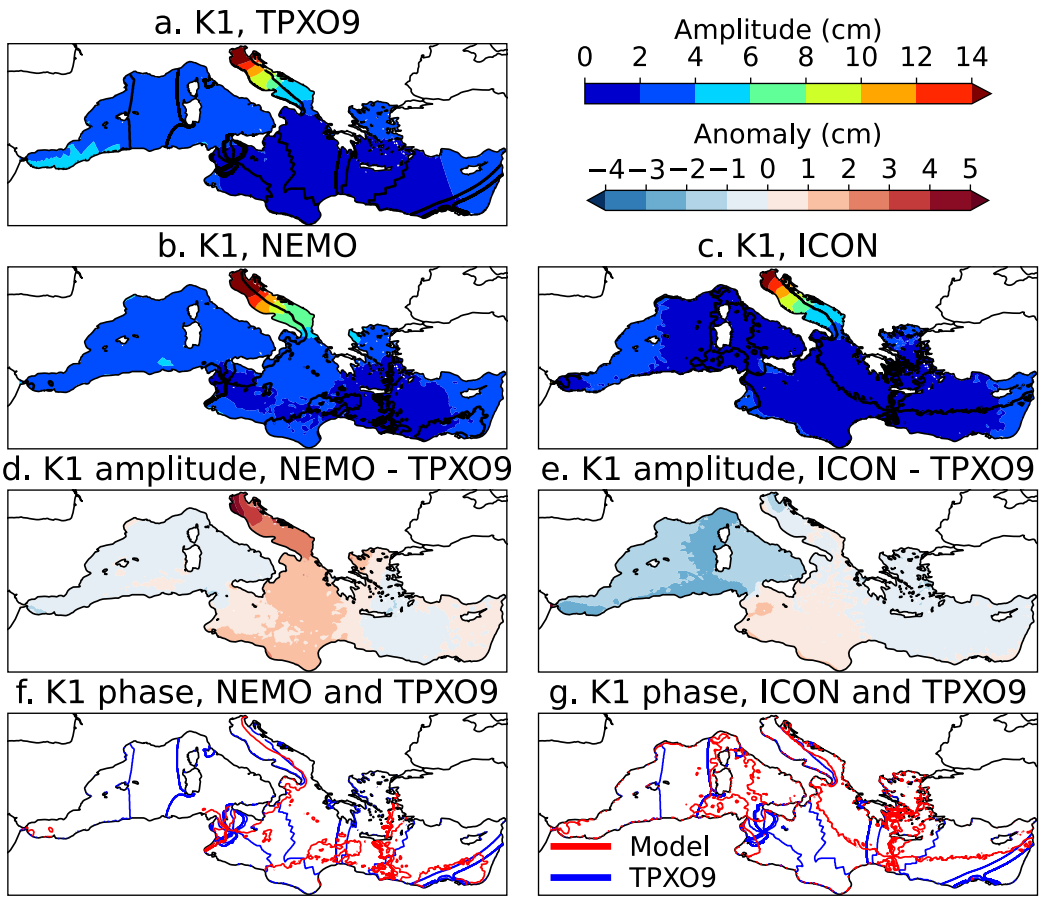

Fig. 3. Amplitude and phase of the K1 tidal component in a. TPXO9, b. NEMO, and c. ICON for March 2022, the amplitude difference between TPXO9 and d. NEMO and e. ICON, and the phase contours of TPXO9 compared to f. NEMO and g. ICON. The phase contours are 30° apart.

for NEMO. It is also valuable to compare the generation of internal tides between diurnal and semidiurnal components, since we know that semidiurnal internal tides can propagate freely in the Mediterranean Sea while diurnal internal tides remain trapped along the bathymetry, due to their respective critical latitudes. Figures equivalent to Figs. 7 and 8 split into the diurnal and semidiurnal components can be found in Appendix C, where it is clear that the differences between NEMO and ICON arise in the diurnal tidal components, while the semidiurnal components have similar internal tide generation in both models.

It should be noted that there are some negative values for C. This is a spurious result that occurs when internal tides generated at a given site interfere with internal tides generated elsewhere, causing ρ' and W to become out of phase and leading to negative values of C. The interference could be stronger in a closed basin than in open ocean (as was analysed in other studies such as Li and von Storch (2020)), due to internal tides reflected at the coasts. We can further quantify internal tide generation by taking an area-weighted sum over each of the regions, although the caveats mentioned above should be considered. To account for the problem of negative values due to interference, only points with positive values are included in the calculation. The area-summed values of the regions in Fig. 8 are in Table 3, giving an estimate of the total energy for internal tide generation in the Mediterranean Sea: 3.31 GW in NEMO and 1.52 GW in ICON. The value for the total C in the global ocean is 1.7 TW according to Müller (2013). The lower value in ICON is due to the smaller generation of diurnal internal tides in the model compared to NEMO, while semidiurnal internal tide generation is similar in both models. This is likely related to differences in the barotropic tides in the models, where semidiurnal tidal amplitude and phase are similar in NEMO and ICON, while the K1 tides are less alike (see Section 3).

Table 3
Area-summed values for C for the Mediterranean Sea and within the regions of Fig. 8, in W. Semidiurnal and diurnal components are shown separately and combined.

	NEMO (W)	ICON (W)
Mediterranean Sea	3.31×10^9	1.52×10^9
Mediterranean Sea (semidiurnal)	0.88×10^9	0.90×10^9
Mediterranean Sea (diurnal)	2.43×10^9	0.61×10^9
Gibraltar Strait	3.39×10^7	3.11×10^7
Gibraltar Strait (semidiurnal)	2.04×10^7	2.02×10^7
Gibraltar Strait (diurnal)	1.34×10^7	1.09×10^7
Sicily Strait/Malta Bank	3.67×10^8	7.45×10^7
Sicily Strait/Malta Bank (semidiurnal)	4.81×10^7	3.31×10^7
Sicily Strait/Malta Bank (diurnal)	3.19×10^8	4.14×10^7
Hellenic Arc	1.38×10^9	7.04×10^8
Hellenic Arc (semidiurnal)	3.61×10^8	4.32×10^8
Hellenic Arc (diurnal)	1.02×10^9	2.73×10^8

4.2. Internal tide propagation

A point-by-point harmonic analysis of the three-dimensional horizontal currents over the 744 h of the model run is carried out in order to isolate tidal currents for each component, using software based on Foreman et al. (2009). From this, a vertical mean is removed to calculate the baroclinic component of this as the internal tide kinetic energy for a single layer.

Maps of vertical mean baroclinic kinetic energy of the M2 and K1 tidal components in the NEMO and ICON experiments are shown in Fig. 9.

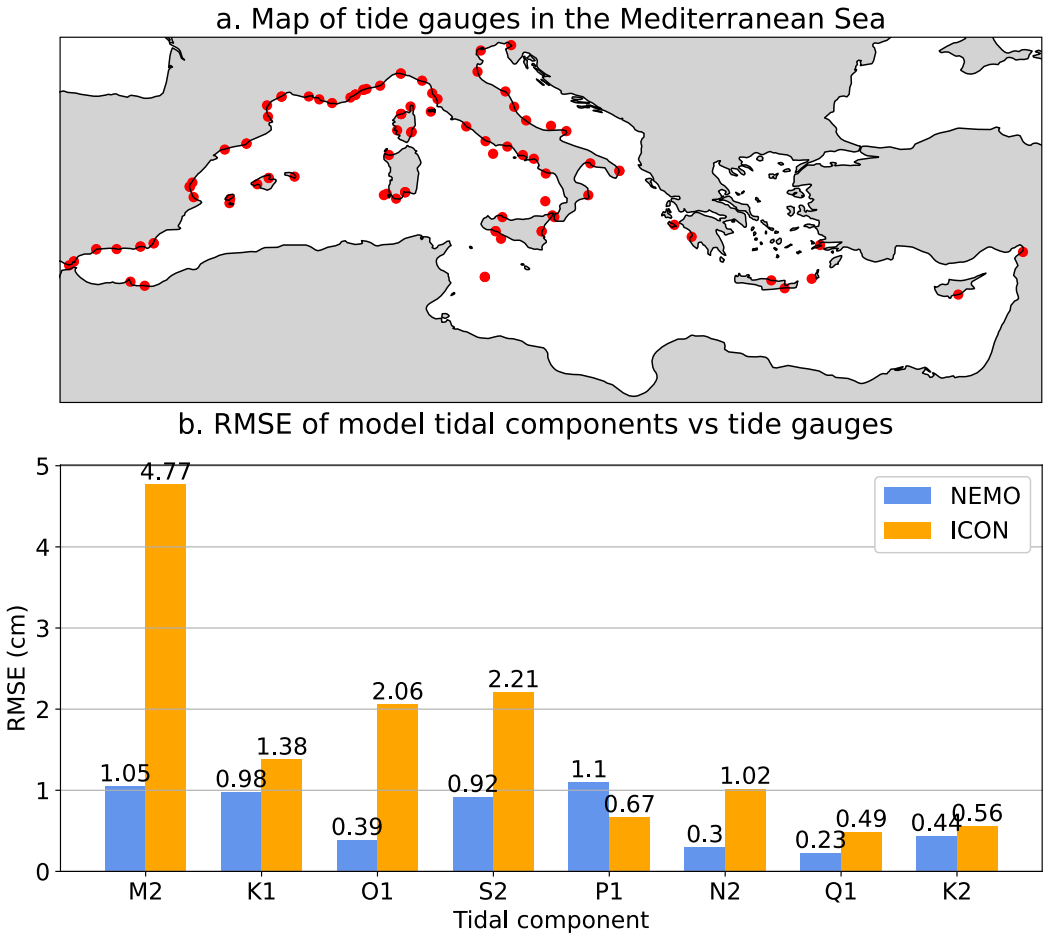

Fig. 4. Map of Mediterranean Sea tide gauges (a) and root mean square misfits of model tides compared to tide gauges (b) for the amplitude and phase of eight tidal components in March 2022. NEMO is in blue and ICON is in orange.

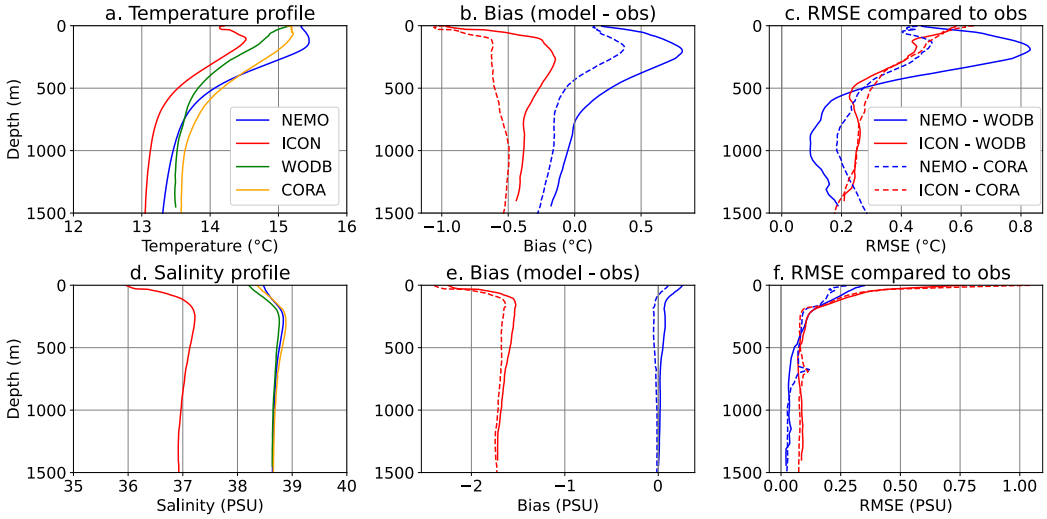

Fig. 5. Vertical profiles for the Mediterranean Sea of a. temperature and d. salinity, for two models: NEMO (blue), ICON (red), and two observational datasets: WODB (Mishonov et al. (2024), green), and CORA (Copernicus Marine Service (2024), orange), with biases (b., e.) and root mean square errors (c., f.) of the models compared to both observational datasets, where the solid lines compare the models to the WODB and the dashed lines show the comparison with CORA.

The vertical mean baroclinic kinetic energy of the M2 component is similar in the two model implementations. The regions with the highest baroclinic kinetic energy through the water column are similar to those identified in previous work, e.g. Morozov et al. (2002); Gasparini et al. (2004); Alford et al. (2012): the Gibraltar Strait, Sicily Channel, and Aegean Sea. Moreover, this analysis highlights sites of internal tide generation or propagation that were not mentioned in previous literature: the northern Adriatic Sea, the Tyrrhenian Sea and the Cretan Passage. The K1 tidal component has a different distribution of baroclinic kinetic energy in the two models, with particularly high kinetic energy in

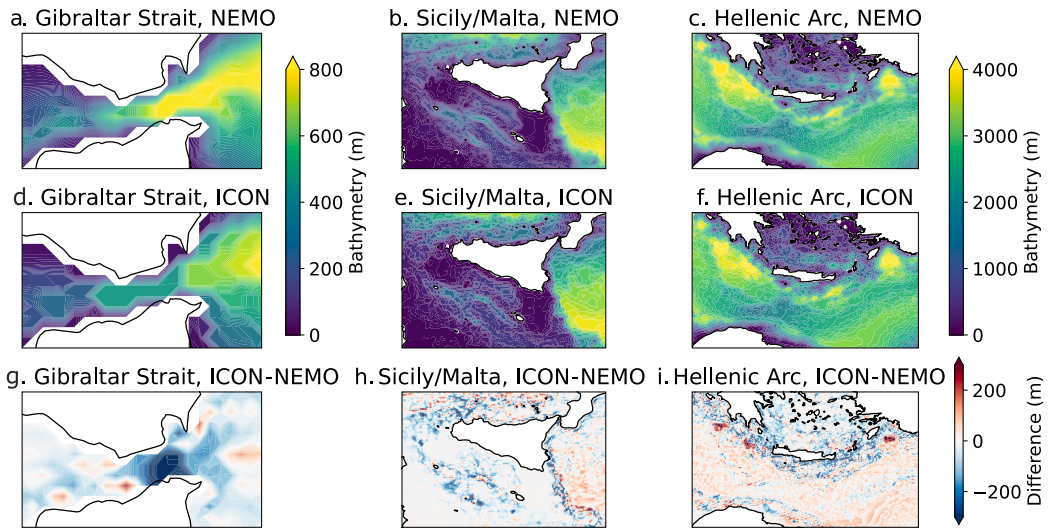

Fig. 6. Model bathymetry in key regions for internal tide generation: Gibraltar Strait/Alboran Sea (a, d, g), Sicily Strait/Malta Bank (b, e, h), and Hellenic Arc (c, f, i), for NEMO (a, b, c), ICON (d, e, f), and the difference between models, ICON - NEMO (g, h, i).

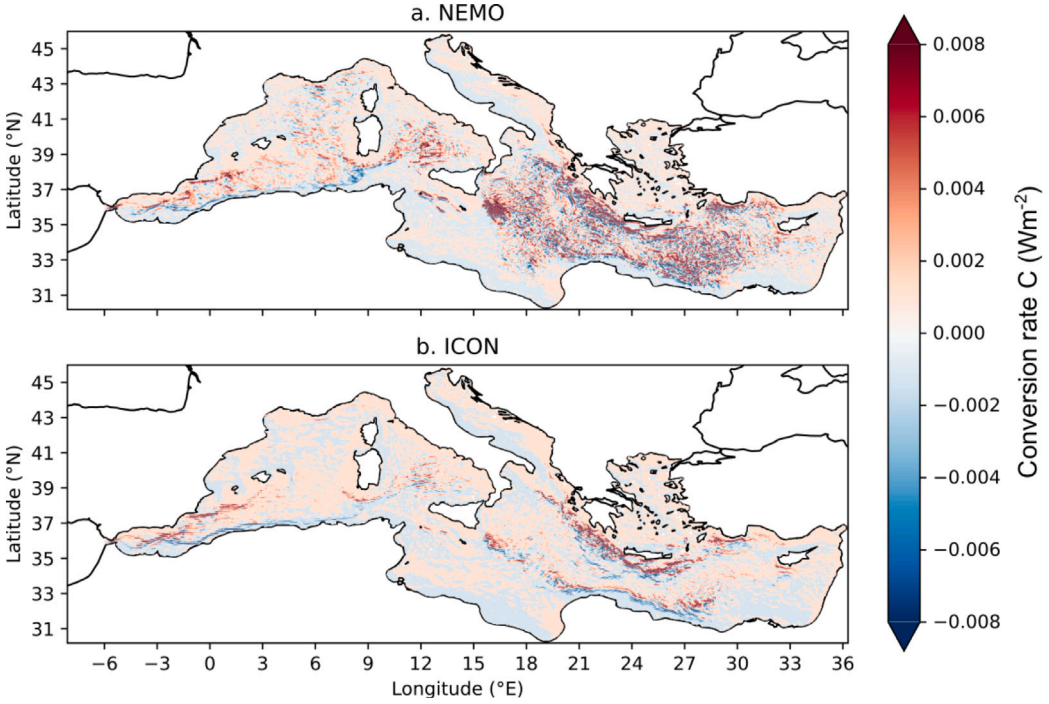

Fig. 7. Maps of the barotropic to baroclinic energy conversion term (C) in the Mediterranean Sea, for a. NEMO, and b. ICON.

NEMO in the southern Adriatic Sea and the Malta Bank (as discussed in Oddo et al., 2023), as well as along the African coast in the south-east of the basin. The K1 baroclinic kinetic energy is larger in NEMO than in the ICON experiment but it appears in broadly similar regions in the two models.

Fig. 10 shows the baroclinic M2 currents at the vertical level closest to 150 m in each model. In both models, the propagation of internal tides is visible in the western Mediterranean inflowing current inside the Gibraltar Strait. This current typically flows from the Gibraltar Strait along the north African coast at depths of 0–150 m, which has particularly clear tidal beams in the baroclinic zonal velocity (Figs. 10a and b). The waves are also seen in the Tyrrhenian Sea, and in several regions of the eastern Mediterranean, most notably to the west of Crete. There are some key differences between the two experiments: the NEMO experiment shows higher kinetic energy in the south-western Mediterranean whereas the ICON experiment has more kinetic energy in the Tyrrhenian Sea, but the regions showing propagating waves and tidal beams are similar in the two models.

These waves at the M2 frequency are also visible at deeper layers: Figs. C.6 and C.7 show the baroclinic M2 currents at 300 m and 1000 m, from which we see the kinetic energy is lower at deeper levels, but tidal beams are still present until around 1000 m, particularly in the Hellenic Arc region where the deep Ionian Sea meets the shallow Aegean Sea, explaining the wave propagation in the Ionian Sea.

Spectra of the baroclinic horizontal currents throughout the water column are plotted at several key points. These are the centres of the

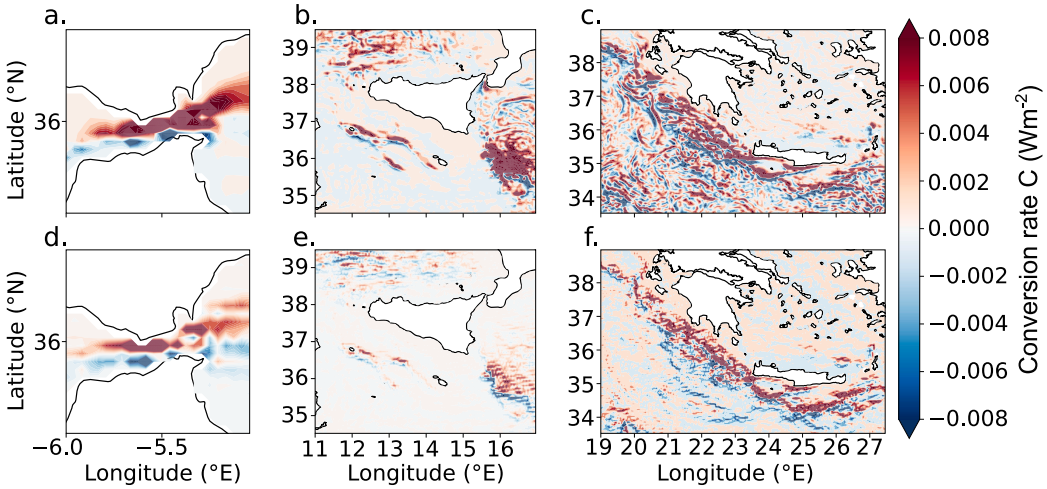

Fig. 8. Maps of the barotropic to baroclinic energy conversion term (C) in key regions of the Mediterranean Sea: the Gibraltar Strait/Alboran Sea (a. NEMO, and d. ICON), the Sicily Strait/Malta Bank (b. NEMO, and e. ICON), and the Hellenic Arc region (c. NEMO, and f. ICON).

regions in Fig. 1, as well as in four further regions, which appear to have internal tide propagation in the maps of Fig. 10. These are the Algerian Sea (37.70°N, 5.23°E), the Tyrrhenian Sea (39.73°N, 11.50°E), and two points in the Ionian Sea (35.90°N, 20.46°E and 33.50°N, 19.48°E), which are the centre points of regions shown in Fig. 1. Three of these eight spectra are shown in Fig. 11: the Gibraltar Strait, Sicily Strait, and northern Ionian Sea, while the others can be found in Appendix D.

In the Gibraltar Strait (Fig. 11a-d), we see high values of energy density at both diurnal and semidiurnal frequencies throughout the water column in both models and for both along-strait (zonal) and cross-strait (meridional) currents. In the Sicily Strait (Fig. 11e-h), the bottom-trapped diurnal internal tide is more prominent, while there is only a small peak of semidiurnal baroclinic energy density demonstrating that the M2 internal tide is relatively important in the western basin, while K1 is more prominent in the central Mediterranean Sea. Contrastingly, in the Ionian Sea (Figs. 11i-l), energy density from the currents depends strongly on depth: the upper layers have energy distributed across many frequencies, while the internal frequency has its peak in deeper layers. As discussed in McDonagh et al. (2024), this region shows some interaction between the diurnal internal tide and near-inertial waves, particularly in NEMO, where the near-inertial peaks stretch towards the diurnal frequency. This analysis of the baroclinic kinetic energy further confirms that the wave-wave interactions seen in McDonagh et al. (2024) refer to interactions between internal tides and near-inertial waves.

4.3. Internal tide wavelengths

Typical wavelengths of the first two modes of the M2 internal tide in the global ocean are 100–160 km and 45–80 km according to Li et al. (2015), while Ray and Zaron (2016) finds that these values are around 100–170 km and 50–80 km for the first two modes respectively. Others find that open-ocean internal tide wavelengths can be at least 200 km (Wunsch, 1975; Carter et al., 2012), while at the coast around 100 km is a reasonable value (Carter et al., 2012). Several regions are chosen for wavenumber analysis, following propagation paths of the M2 internal tide seen in Fig. 10. Fig. 1 includes a map of these new analysis regions. Wavenumber spectra of the tidal baroclinic velocity of the M2 component is calculated along these paths using the periodogram as described in Appendix A. The data used to calculate the periodogram is from the harmonic analysis of baroclinic currents for each tidal component, along the length of the paths of the blue highlighted boxes in Fig. 1. Several parallel lines (five for the Algerian Sea, ten for the other regions) are averaged after the periodogram is calculated for each line.

Table 4
Wavelengths of the first baroclinic mode of the M2 internal tide in the regions from Figs. 1 and 12, calculated by solving the Sturm–Liouville eigenvalue problem.

Region	NEMO (km)	ICON (km)
Algerian Sea (Fig. 12a–c)	71.6	54.7
Tyrrhenian Sea (Fig. 12d–f)	57.5	45.8
Ionian Sea (north) (Fig. 12g–i)	52.0	43.3
Ionian Sea (south) (Fig. 12j–l)	53.3	41.3

The wavenumber spectra for the M2 component along each of these paths are in Fig. 12, with additional data from a similar NEMO configuration without tides (the non-tidal configuration used in McDonagh et al., 2024). In Fig. 12, the largest density peak in the Tyrrhenian and northern Ionian seas are at wavelengths greater than 200 km. These can be attributed to seiches in the Mediterranean Sea, which include modes at frequencies close to that of the M2 tidal component, at 11.4 h and 12 h (Schwab and Rao, 1983; Lozano and Candela, 1995), which are known to interact with tides (McDonagh et al., 2024). The peak most relevant to internal tides is at around 50–100 km and is visible in the Algerian Sea and Ionian Sea, in both experiments but most prominently NEMO. This is the first vertical mode of the M2 internal tide. A second mode also appears in Fig. 12b and e, at a higher wavenumber than the first, close to 50 km.

These results from model outputs are also compared to theoretical values for the first mode of the M2 internal tide in the same regions, calculated by solving the Sturm–Liouville eigenvalue problem, assuming a flat bottom within each region at its area-weighted mean depth. Table 4 shows these results for both models. In most of the regions analysed, these calculated wavelengths are well-matched with those in the spectra. It also helps us to differentiate between the peaks due to internal tides in Fig. 12 and other peaks which are arising from other phenomena at frequencies close to that of the M2 tide, such as seiches. We argue now that the longer wavelength peaks in the Tyrrhenian and Ionian Seas are not due to tides but to seiches that are at similar frequencies. The calculated wavelengths in Table 4 are shorter in ICON than in NEMO in all four analysed regions. This can be attributed to the Brunt-Väisälä frequency differences between the models: in the critical depths for internal tides of around 100–1000 m, NEMO is more stratified than ICON in these regions of interest (see Appendix C), which has a relation with the wavelength according to

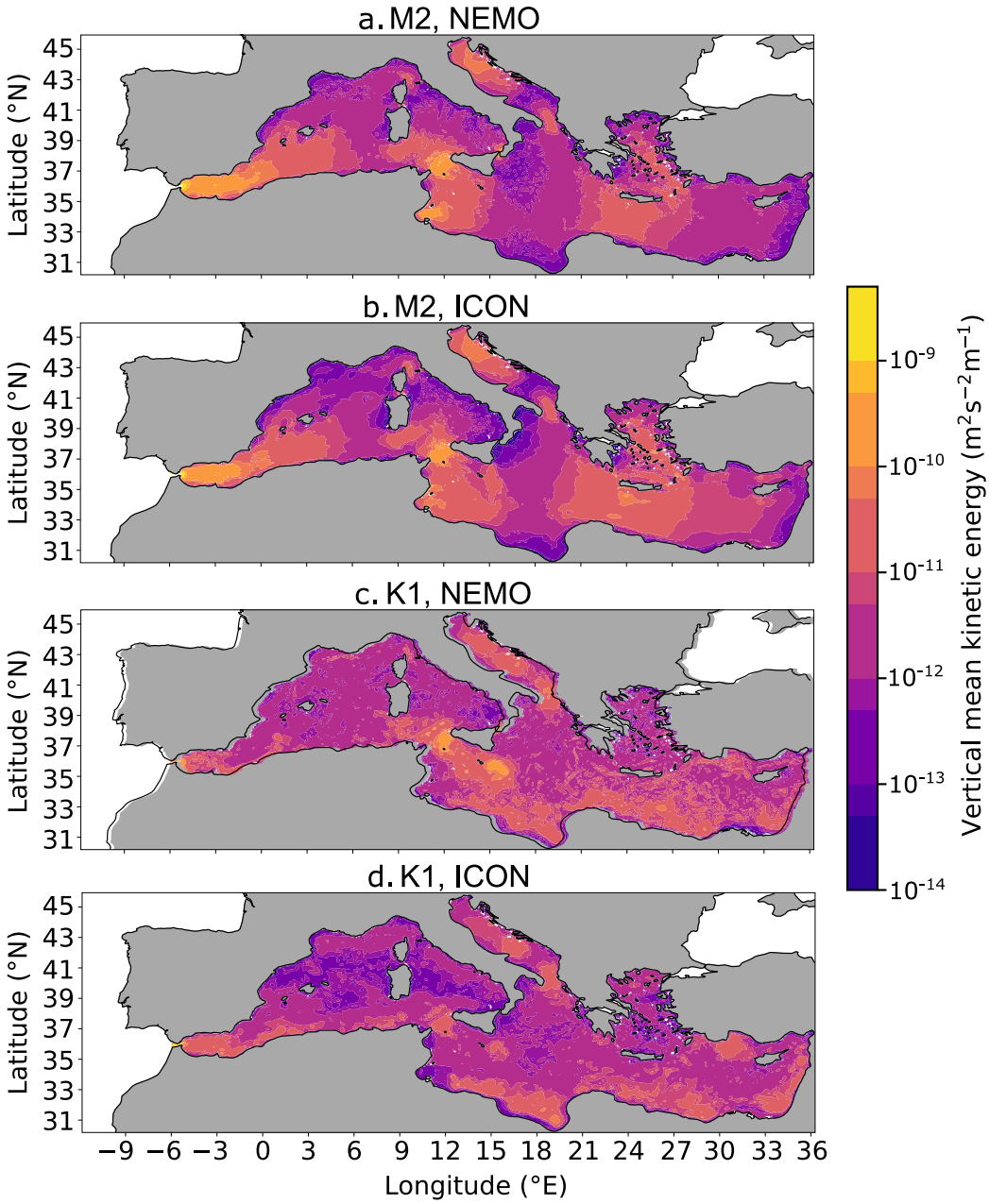

Fig. 9. Vertical mean baroclinic kinetic energy in the Mediterranean Sea during March 2022, for the M2 component in a. NEMO and b. ICON and for the K1 component in c. NEMO and d. ICON.

the equations in Appendix B, where more details on the Sturm–Liouville eigenvalue problem and its associated assumptions can be found.

5. Conclusions

For the first time, internal tides in the Mediterranean Sea are mapped in the whole basin (Figs. 7–10). Three major generation sites are found: firstly, the Gibraltar Strait and Alboran Sea, secondly, the Sicily Strait and Malta Bank in the central Mediterranean Sea, and finally, the Hellenic Arc, as well as several minor generation sites in the Eastern Mediterranean more broadly, and the Tyrrhenian Sea. Both diurnal and semidiurnal internal tides are analysed, with a particular focus on the M2 and K1 components. The two components have varying importance in different regions, with M2 being more prominent in the Western Mediterranean Sea and Cretan Passage, and K1 being most important in the central and southeastern parts of the basin. Semidiurnal internal tides propagate for up to hundreds of kilometres in the Mediterranean Sea, both in the eastern and western basins, particularly in the Algerian Sea, Tyrrhenian Sea, and Ionian Sea, which respectively propagate from the three key generation sites listed above. The first modes of the M2 internal tide are resolved by the numerical models and have wavelengths comparable to Li et al. (2015) in the NEMO experiment, whereas the ICON-O simulation has shorter wavelengths than suggested by the literature in several regions, which is likely due to differences in the stratification profiles of the two models, particularly at the Gibraltar Strait, since the Algerian Sea wavelengths are particularly different in the two models.

The two numerical experiments have similar generation sites and propagation regions for internal tides, but the specific wavelengths, the propagation directions, and the propagation distances vary between the two experiments. Some reasons for this include differences in stratification, model bathymetry, and the representation of barotropic tides, as well as differing configurations of key regions such as the Gibraltar

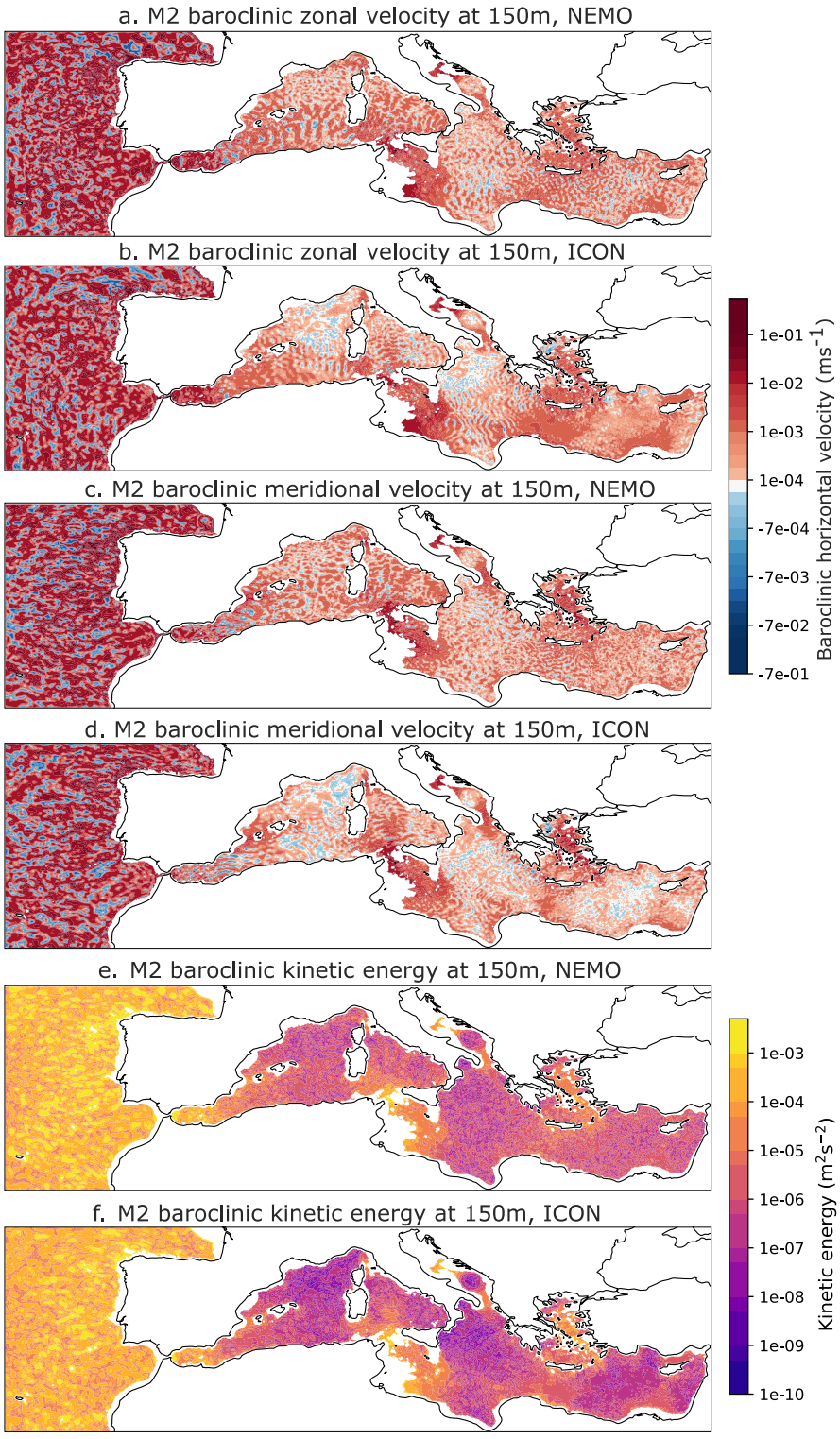

Fig. 10. Maps of baroclinic M2 current amplitude at the closest vertical level to 150 m for a. zonal velocity component in NEMO, b. zonal velocity component in ICON, c. meridional velocity component in NEMO, d. meridional velocity component in ICON, e. kinetic energy in NEMO, and f. kinetic energy in ICON.

Strait between the two model implementations. The barotropic tidal amplitudes and phases provided by the NEMO and ICON experiments are compared to a global barotropic model used as a Ref. (Egbert and Ray, 2003) in Section 3. However, further validation using data from cruises in some isolated regions, such as that of Oddo et al. (2023), could be used to better understand which model has a more correct representation of internal tides through direct observations.

This work was a first step in mapping internal tides throughout the Mediterranean basin using a high-resolution numerical model. Next steps for the study of internal tides in the Mediterranean Sea could include an analysis of interactions with other mesoscale phenomena, particularly near-inertial waves, as was briefly discussed in McDonagh et al. (2024) as well as in this work, and the interaction between internal tides and mesoscale eddies, which are a key feature in the

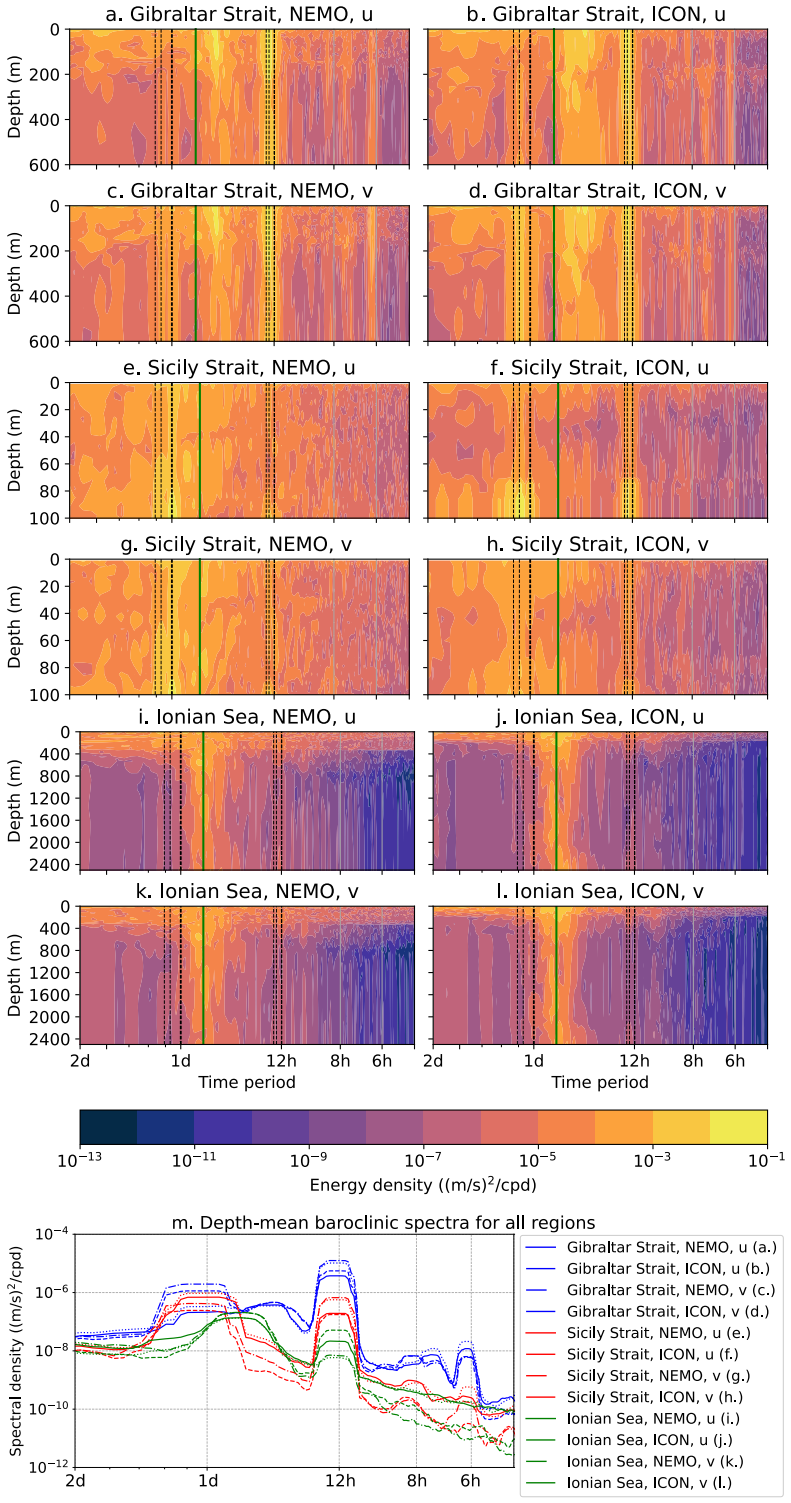

Fig. 11. Spectra of zonal (u) and meridional (v) currents at three points: the Gibraltar Strait (35.98°N, 5.48°W) (a–d), Sicily Strait (37.19°N, 11.98°E) (e–h), and Ionian Sea (35.73°N, 20.44°E) (i–l), evaluated from NEMO (left) and ICON (right) model simulations through the vertical column. Dashed black lines represent the tidal frequencies included in NEMO and the green line indicates the inertial frequency at the latitude of the point. m. Depth-mean spectra of each of the above panels.

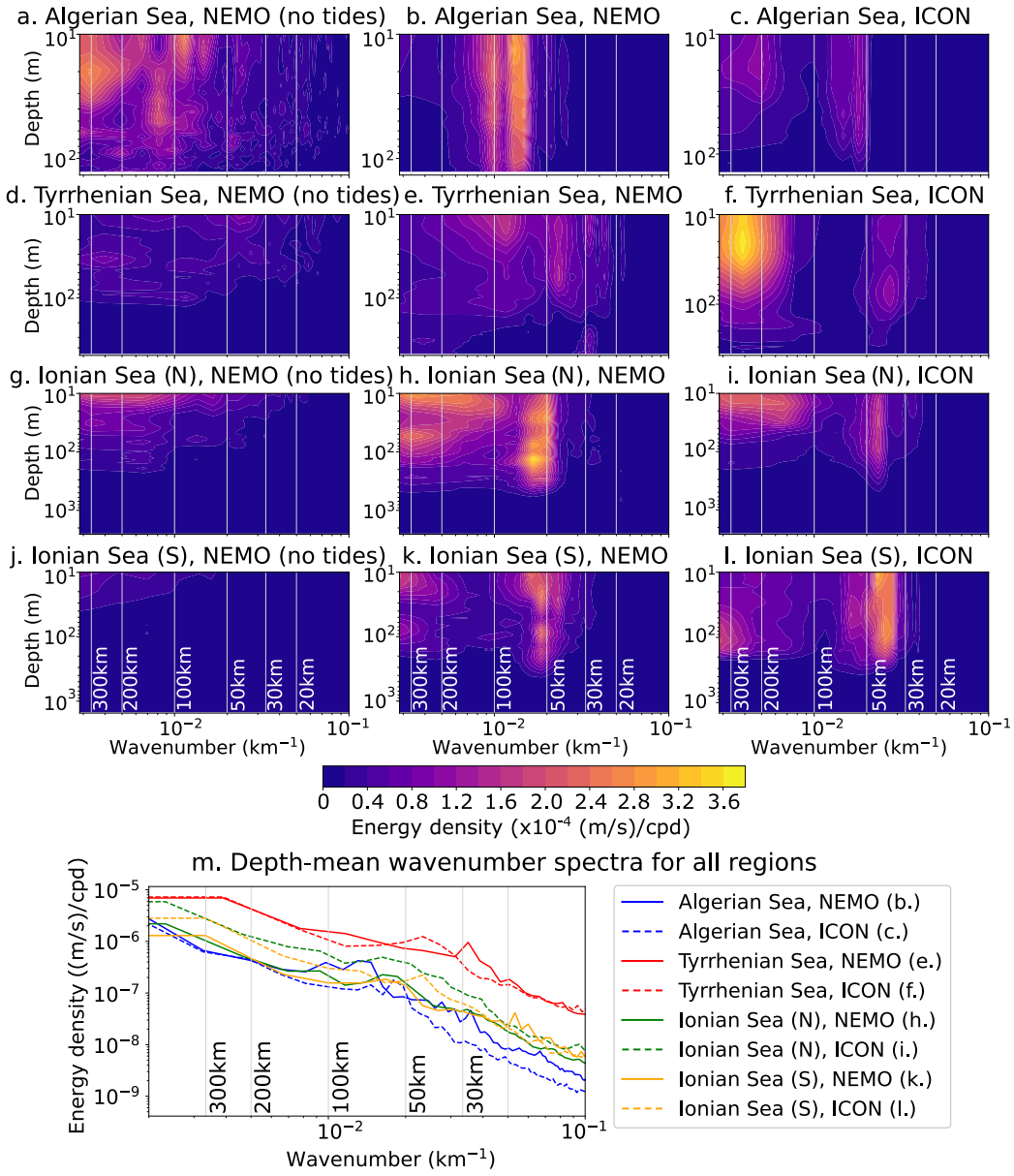

Fig. 12. Wavenumber energy density spectra of M2 baroclinic currents for four regions (as in Fig. 1): a–c. Zonal velocity, Algerian Sea (37.70°N, 0.48°W–9.98°E), NEMO (without tides), NEMO and ICON, d–f. Meridional velocity, Tyrrhenian Sea (37.98–41.48°N, 11.50°E), NEMO (without tides), NEMO and ICON, g–i. Zonal velocity, Ionian Sea (north) (35.90°N, 17.98–22.94°E), NEMO (without tides), NEMO and ICON, j–l. Zonal velocity, Ionian Sea (south) (33.50°N, 15.98-22.98°E), NEMO (without tides), NEMO and ICON, m. depth-averaged spectra for all regions.

Mediterranean Sea circulation. Another phenomenon of interest would be any interaction between internal tides and seiches, which are important in the Mediterranean Sea dynamics. It is possible that internal tides could be generated in other regions of steep topography such as small islands and seamounts, and narrow straits such as the Messina Strait, which are not properly resolved by the model implementations used in this work. A regional study of the central Mediterranean Seas with sub-kilometre scale horizontal resolution would be a particularly useful step in understanding the internal tides in this region. Moreover, the Gibraltar Strait, although resolved in both of the models used in this work, generally needs a horizontal resolution of at least 500 m to properly resolve its physics (Sannino et al., 2009). Future studies should consider the use of sub-kilometre scale models, nested models, or unstructured grid models to better understand the internal wave field in this small and complex region.

CRediT authorship contribution statement

Bethany McDonagh: Writing – review & editing, Writing – original draft, Visualization, Formal analysis, Data curation. **Jin-Song von Storch:** Writing – review & editing, Supervision, Formal analysis, Data curation. **Emanuela Clementi:** Writing – review & editing, Supervision, Data curation. **Nadia Pinardi:** Writing – review & editing, Supervision, Formal analysis, Conceptualization.

Declaration of competing interest

The authors declare that they have no known competing financial interests or personal relationships that could have appeared to influence the work reported in this paper.

Acknowledgements

This research was funded under the contract for the Mediterranean Sea Monitoring and Forecasting Centre (Contract No. 24252L05-COP-MFC MED-5200) within the Copernicus Marine Service, funded by the European Union, implemented by Mercator Ocean International. The study also included support from the University of Bologna Ph.D. programme in Future Earth, Climate Change and Societal Challenge. JSvS thanks the support from TRR 181 funded by the DFG (German Research Foundation, project no. 274762653).

Appendix A. Spectral analysis

In this work, spectra are calculated to analyse the frequencies and wavelengths at which internal tides are generated and propagated at a variety of temporal and spatial scales. In the following sections, each type of spectrum is briefly defined.

A.1. Spectrum calculation

For all spectra, a periodogram is used as an estimate of the spectrum. The main advantages of using the periodogram over other estimators of a spectrum is that a periodogram is asymptotically unbiased, and estimates at adjacent frequencies are almost uncorrelated. The periodogram is calculated as follows:

For a timeseries $x_1, \dots, x_T$, where $x_t, t = 1, \dots, T$ is periodic and can be expanded in terms of sine and cosine functions, x_t is;

$$x_t = a_0 + \sum_{j=1}^{q} (a_j \cos(2\pi\omega_j t) + b_j \sin(2\pi\omega_j t)), \omega_j = \frac{j}{T}, j = 1, \dots, q, q = \frac{T^*}{2} \quad \text{(A.1)}$$

where T^* is the largest integer within $T/2$, and

$$a_0 = \frac{1}{T} \sum_{t=1}^{T} x_t \quad \text{(A.2)}$$

$$a_j = \frac{2}{T} \sum_{t=1}^{T} x_t \cos(2\pi\omega_j t) \quad \text{(A.3)}$$

$$b_j = \frac{2}{T} \sum_{t=1}^{T} x_t \sin(2\pi\omega_j t) \quad \text{(A.4)}$$

The periodogram at the frequency ω_j is then:

$$I_{T_j} = \frac{T}{4}(a_j^2 + b_j^2), j = \frac{T^* - 1}{2}, \dots, \frac{T^*}{2}. \quad \text{(A.5)}$$

This periodogram is used to estimate power spectra from timeseries at single points in the ocean.

A.2. Wavenumber spectrum

In addition to spectra in frequency space, wavenumber spectra are calculated to find the wavelengths of the internal tides. These spectra

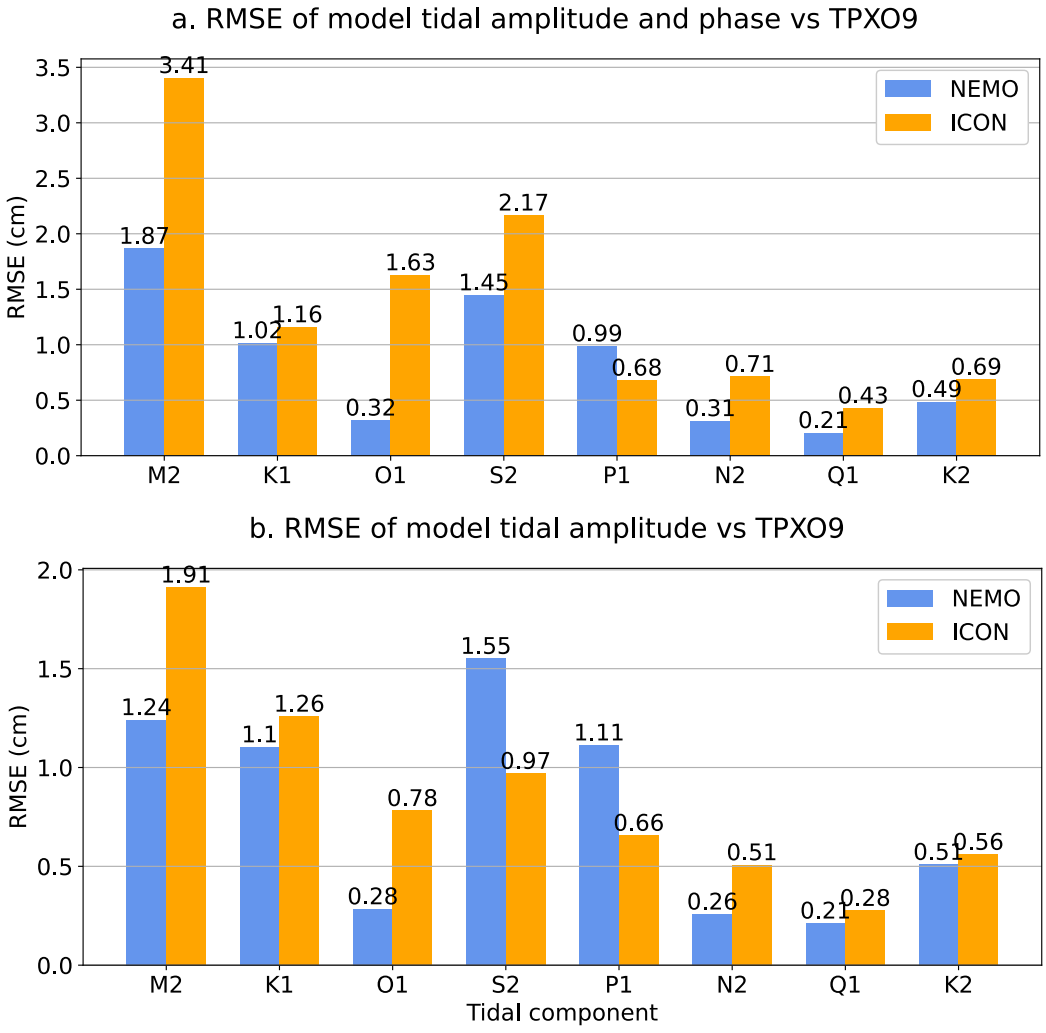

Fig. C.1. Root mean square error of model tidal amplitude and phase (a) and amplitude-only (b) for eight tidal components compared to TPXO9 in the Mediterranean Sea for March 2022. NEMO is in blue and ICON is in orange.

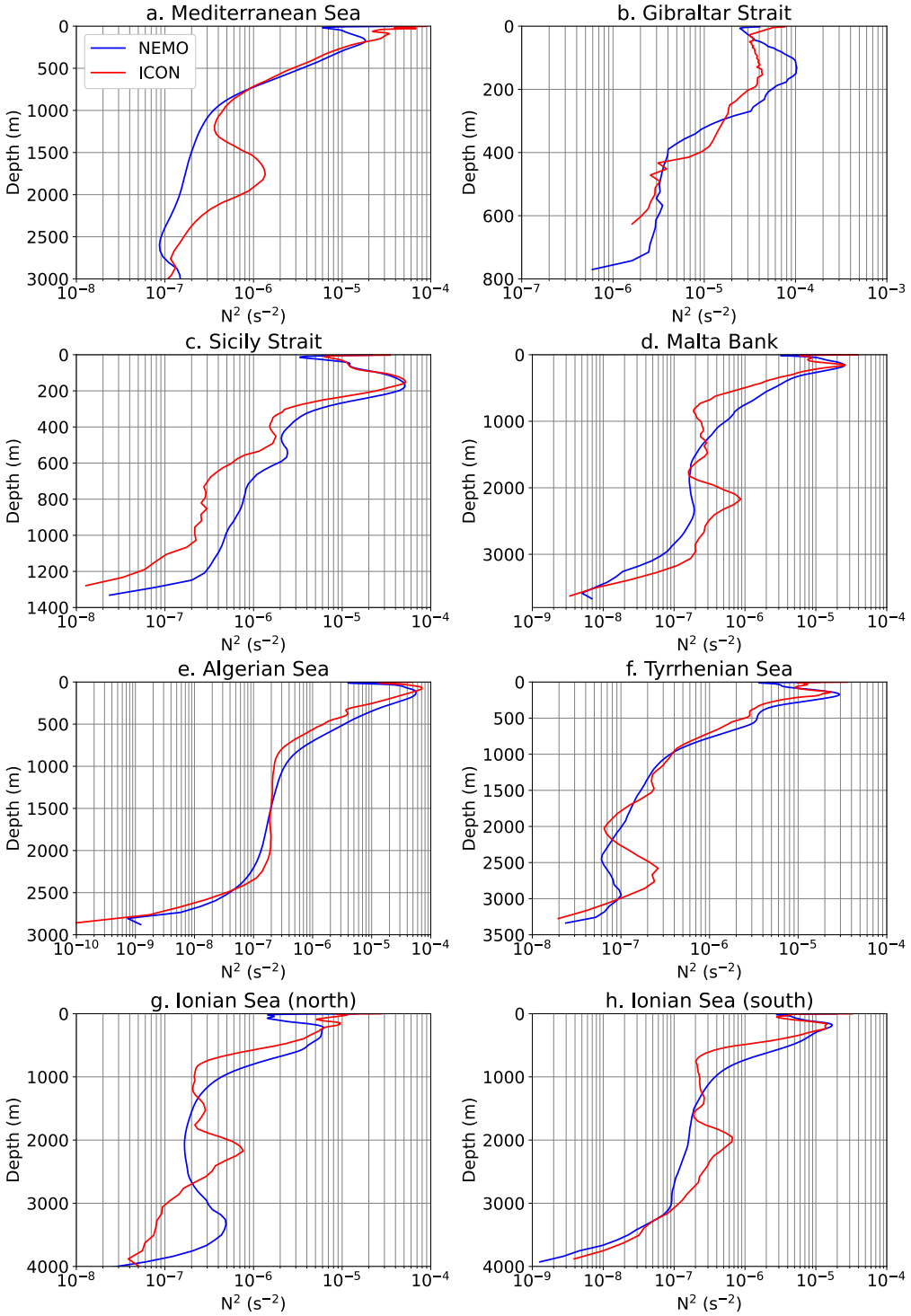

Fig. C.2. Vertical profiles of the squared Brunt-Väisälä frequency for the NEMO simulation (blue) and the ICON simulation (red), for a. the Mediterranean Sea, and the regions shown in Fig. 1. These are b. the Gibraltar Strait (35.7–36.3°N, 6.0–5.3° W), c. Sicily Strait (36.5–38.0°N, 11.0–13.0°E), d. Malta Bank (35.0–37.0°N, 13.0–16.0°E), e. Algerian Sea (37.70°N, 0.48–9.98°E), f. Tyrrhenian Sea (38.98–41.48°N, 11.50°E), g. Ionian Sea (north) (35.90°N, 17.98-22.94°E), and h. Ionian Sea (south) (33.50°N, 15.98–22.98°E). Note that the axes are not the same in each sub-plot, which are cropped to the relevant depth scales and N^2 ranges.

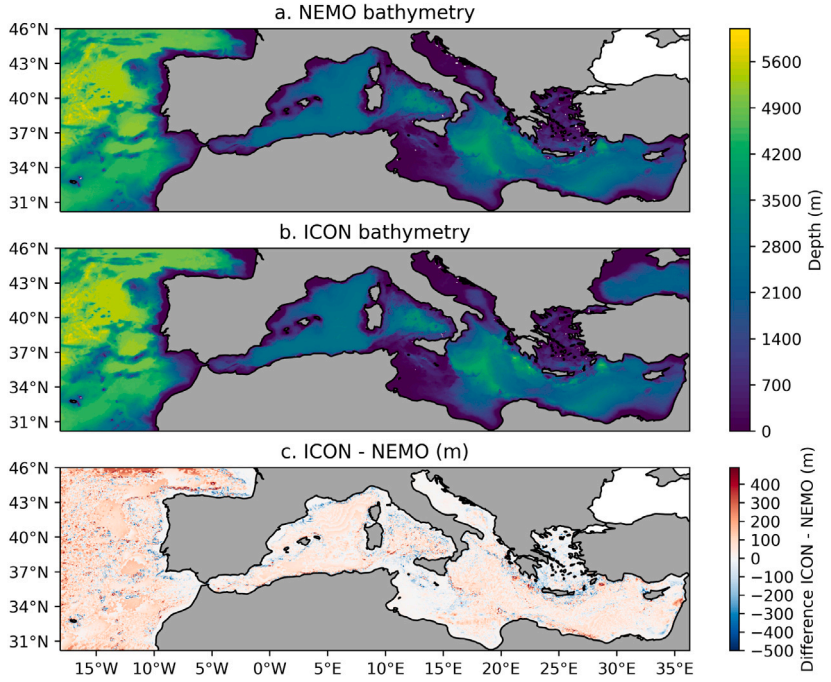

Fig. C.3. Model bathymetry for a. NEMO, b. ICON, and c. Difference (ICON - NEMO).

are calculated in wavenumber space, along a length of physical space at a specific time, rather than in frequency space using a time series of data. The periodogram is also used for this calculation, replacing the frequency ω_j with the wavenumber k_j and the time period T with wavelength λ. A harmonic analysis of currents for each tidal component is used to calculate the periodogram, to analyse the wavelengths at tidal frequencies.

Appendix B. The Sturm–Liouville eigenvalue problem

Solutions to the Sturm–Liouville eigenvalue problem allow us to calculate the wavelengths of internal tides to compare to the low mode internal tide wavelengths found through wavenumber analysis (see Section 3.3) and confirm that the peaks found through wavenumber analysis are indeed due to internal tides. The Sturm–Liouville problem uses the squared Brunt-Väisälä frequency from the model outputs, interpolated onto a regular vertical grid with a 1 m resolution. The eigenvalue problem is defined as:

$$\frac{1}{N^2}\frac{d^2}{dz^2}w_m(z) = -v_m w_m, m = 1, 2, \ldots \tag{B.1}$$

where z represents the vertical axis, N^2 is the squared Brunt-Väisälä frequency, w_m is the eigenvector, and v_m is the eigenvalue of the mth vertical mode. The eigenvalues are then used to calculate the wavelength of the internal tide, L_m by:

$$L_m = \frac{1}{\sqrt{v_m(\omega^2 - f^2)}} \tag{B.2}$$

where ω is the frequency of the internal tide, and f is the Coriolis parameter.

There are several assumptions that are made when using this method to calculate the wavelength of internal tides, primarily that a flat bottom is assumed. Due to the high resolution of the models used in this work, this assumption is significant and is a caveat to this analysis. Moreover, we also neglect any possible variations in stratification and internal tide wavelength within a selected region, which is likely to have varying importance depending on the region and the depth.

Appendix C. Additional analysis

Some supplementary figures which are referred to in Section 4 are displayed here.

C.1. Model validation

In addition to the validation of tides compared to tide gauges (Fig. 4), here we show an equivalent figure comparing each tidal component to TPXO9 data. The root mean square differences between the models and TPXO9, for both amplitude and phase of all eight tidal components included in the NEMO implementation, are shown in Fig. C.1. As is the case for the comparison with tide gauges, most tidal components have a lower RMSE in NEMO compared to ICON. The exceptions to this are the P1 component, in both amplitude and phase, and the amplitude-only RMSE in the S2 component. In the two components of the most interest in this study, M2 and K1, NEMO outperforms ICON when comparing to TPXO9.

The stratification of the ocean is known to affect the propagation of internal tides, where a more stratified ocean allows for greater propagation. Following the comparison of temperature and salinity profiles (Fig. 5), the profiles of the squared Brunt-Väisälä frequency are shown in Fig. C.2. Beginning with the basin-mean profile (Fig. C.2a.), ICON has higher stratification than NEMO through most of the profile, most notably in the first 200 m and below 1000 m. The shape of the two profiles also differs: the profile from the ICON simulation has a second peak at around 1750 m, while the NEMO experiment profile only has a subsurface peak. A Mediterranean Sea observed profile such as those in Cuypers et al. (2012) typically looks more like that of the NEMO experiment, with only one peak close to the surface, whereas the ICON experiment's profile has a double peak which appears more like a typical Atlantic Ocean profile such as those from Emery et al. (1984). This could cause a higher or overestimated propagation of internal tides in ICON when compared to NEMO since ICON is more stratified in several key regions for internal tide propagation. However, at the depths between 200–1000 m, NEMO has a higher stratification. These are among the depths where much of the internal tide propagation occurs (see the Results section), so the difference is notable here even

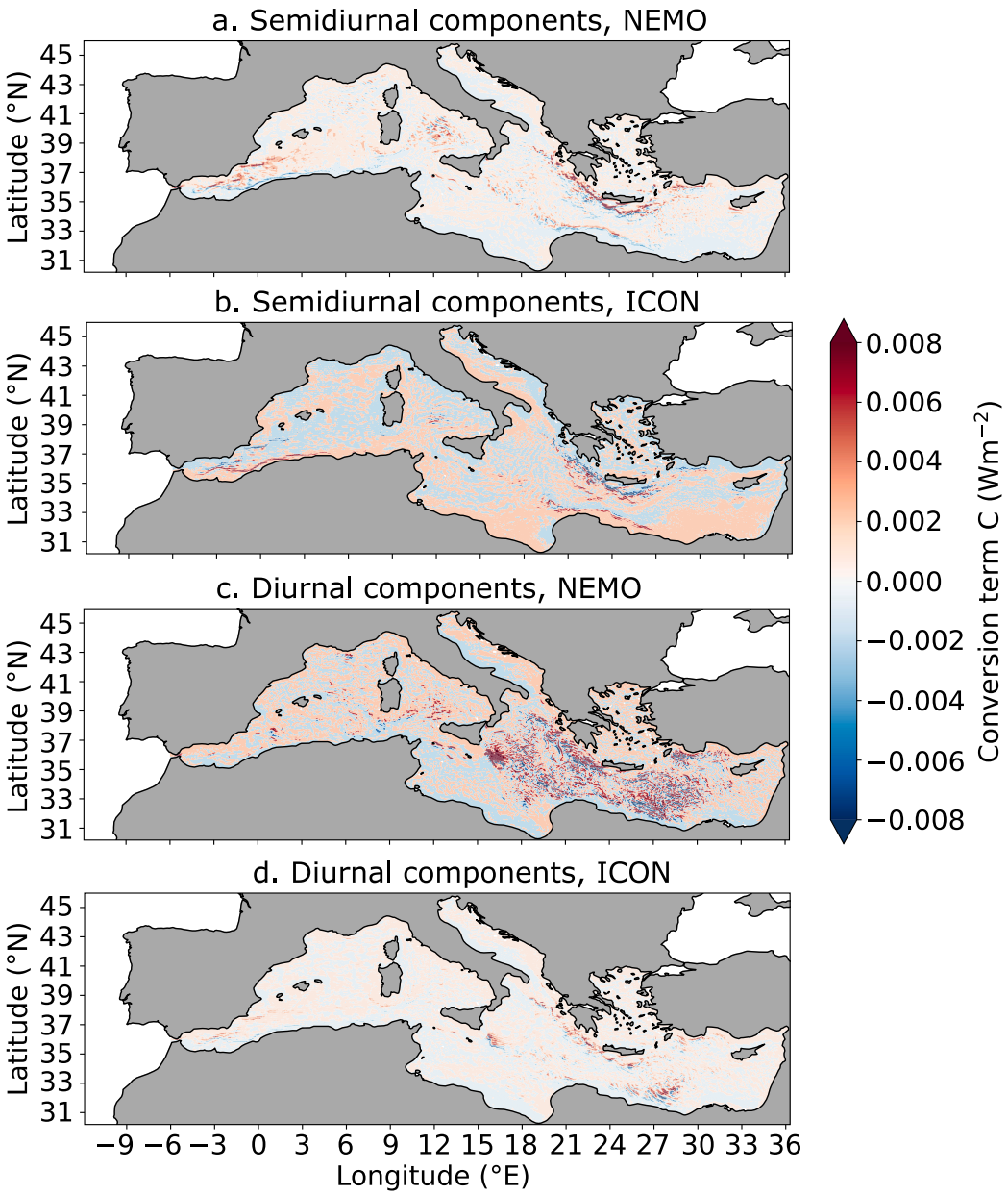

Fig. C.4. Maps of the barotropic to baroclinic energy conversion term (C) in the Mediterranean Sea, split into semidiurnal (M2, S2, K2, and N2; a. NEMO and b. ICON) and diurnal (K1, O1, P1, and Q1; c. NEMO and d. ICON) components.

though it is relatively small compared to the differences between the profiles below 1000 m.

The basin mean profile is not representative of all of the regions of interest in this study, as is clear from Fig. C.2b.-h.. In the Gibraltar Strait, ICON is missing the deeper levels entirely: it is not well-tuned for this region so the bathymetry is not well-resolved. In the upper layers, NEMO has higher stratification than ICON, meaning that the incoming tides from the Atlantic Ocean may propagate further into the western Mediterranean Sea as an internal tide. NEMO is also more stratified than ICON in the upper 1000 m in the Algerian and Tyrrhenian Seas. In the Sicily-Malta region, both profiles are very similar in the upper 200 m, and ICON becomes more unstable compared to NEMO in the 200–1200 m layer. Below 2000 m, ICON becomes more stratified again, but at this depth, there is not much space for internal tides to propagate over long distances due to the steep bathymetry in this region, so these depths are unlikely to be relevant for internal tide propagation in the Mediterranean Sea. In the Eastern Mediterranean, NEMO is an order of magnitude more stratified in the intermediate layers to 1200 m than ICON, again indicating that internal tides are more likely to propagate here in NEMO than in ICON. At around 2000 m in the Ionian Sea, as well as in the Tyrrhenian Sea, we see the aforementioned second peak in ICON which does not appear in NEMO.

Bathymetry is a major indicator for internal tide generation sites, and the bathymetry of key regions is already shown in Fig. 6. The bathymetry over the entire model domain is shown in Fig. C.3.

C.2. Internal tide generation by tidal component

Figs. 7 and 8 show the internal tide generation rate, C, for all tidal components. It is also valuable to compare the generation of internal tides between diurnal and semidiurnal components, since we know that semidiurnal internal tides can propagate freely in the Mediterranean Sea while diurnal internal tides remain trapped along the bathymetry, due to their respective critical latitudes. Fig. C.4 shows the maps from

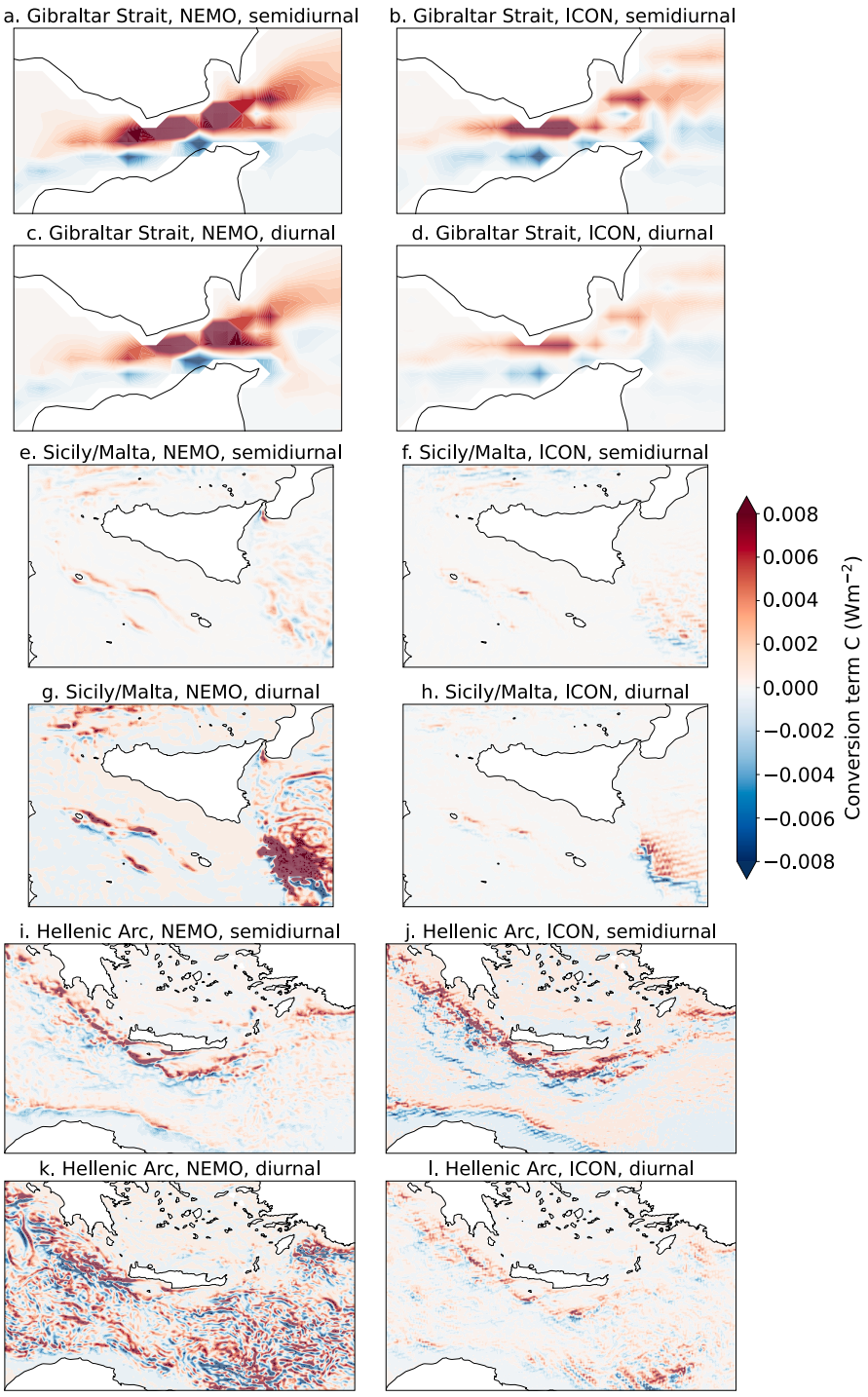

Fig. C.5. Maps of the barotropic to baroclinic energy conversion term (C) in key regions of the Mediterranean Sea: the Gibraltar Strait/Alboran Sea (a.-d.), the Sicily Strait/Malta Bank region (e.-h.), and the Hellenic Arc (i.-l.). Each of these has a panel for NEMO-semidiurnal (a., e., i.), ICON-semidiurnal (b., f., j.), NEMO-diurnal (c., g., k.) and ICON-diurnal (d., h., l.).

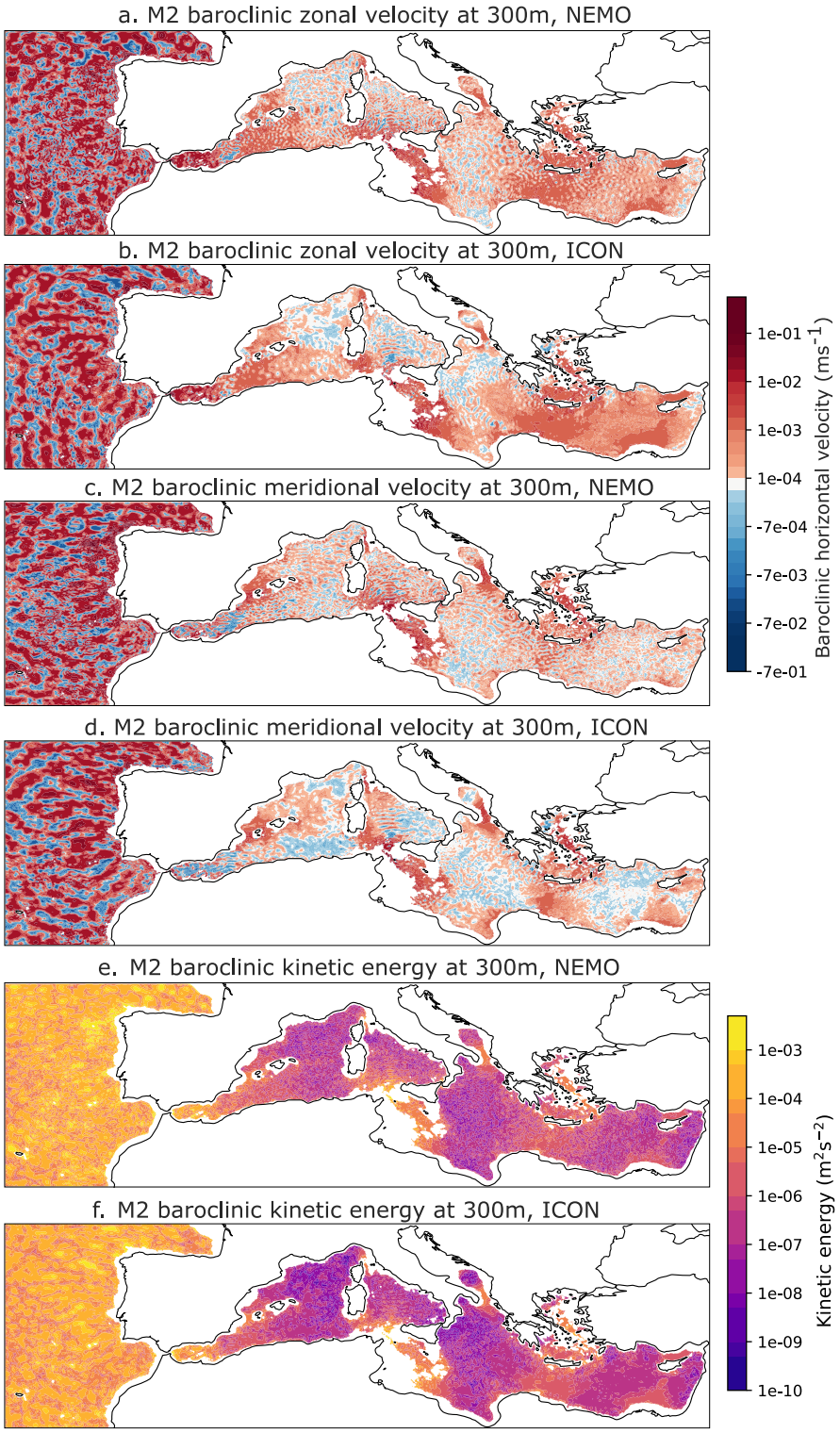

Fig. C.6. Maps of baroclinic M2 current amplitude at the closest vertical level to 300 m for a. zonal velocity component in NEMO, b. zonal velocity component in ICON, c. kinetic energy in NEMO, and d. kinetic energy in ICON.

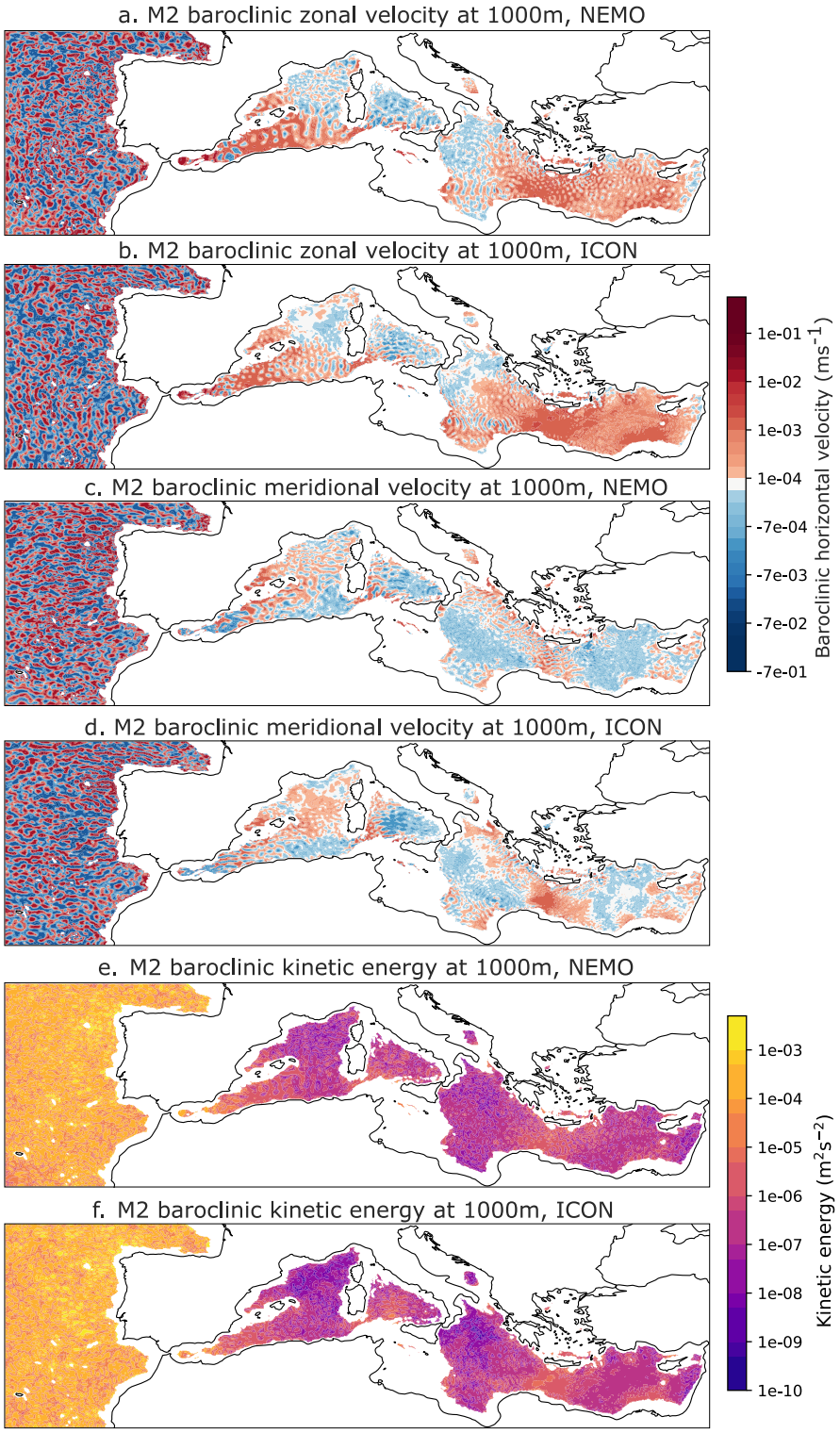

Fig. C.7. Maps of baroclinic M2 current amplitude at the closest vertical level to 1000 m for a. zonal velocity component in NEMO, b. zonal velocity component in ICON, c. kinetic energy in NEMO, and d. kinetic energy in ICON.

Fig. 7 split into diurnal and semidiurnal components, and in Fig. C.5, a component-split version of Fig. 8 is presented. The regions with high values of C are similar for the semidiurnal components in the two experiments, with the key generation sites in the Gibraltar Strait and Hellenic Arc prominent in both models, while the diurnal components are much more widespread in the Eastern Mediterranean in NEMO than they are in ICON: we argue that the diurnal internal tide generation is the primary reason for the model differences. In NEMO, internal tide generation occurs over large swathes of the Eastern Mediterranean, with a strong generation site at the Malta Bank, as expected from Oddo et al. (2023).

C.3. Kinetic energy and propagation of internal tides

Figs. C.6 and C.7 demonstrate the propagation of internal tides in the intermediate and deeper levels of the Mediterranean Sea, in addition to the 150 m layer shown in 10. It is clear that the long-distance propagation of internal tides continues beyond 300 m and reduces at around 1000 m. At this level, the Sicily Strait is closed and the east and western basins are smaller in size, which allows for less propagation than in the intermediate layers. The Hellenic Arc generation site is an exception to this: tidal beams propagating from here into the deep Ionian Sea are still visible at 1000 m.

Appendix D. Supplementary data

Supplementary material related to this article can be found online at https://doi.org/10.1016/j.pocean.2025.103647.

Data availability

The datasets used for this analysis can be found at https://doi.org/10.5281/zenodo.17949665.

References

Alford, M.H., Gregg, M.C., Zervakis, V., Kontoyiannis, H., 2012. Internal wave measurements on the Cycladic Plateau of the Aegean Sea. J. Geophys. Res. 117, C01015. http://dx.doi.org/10.1029/2011JC007488.

Arbic, B.K., 2022. Incorporating tides and internal gravity waves within global ocean general circulation models: A review. Progr. Ocean. 206 (102824), http://dx.doi.org/10.1016/j.pocean.2022.102824.

Baines, P.G., 1982. On internal tide generation models. Deep. Sea Res. Part A. Ocean. Res. Pap. 29 (3), 307–338.

Becker, J.J., Sandwell, D.T., Smith, W.H.F., Braud, J., Binder, B., Depner, J., Fabre, D., Factor, J., Ingalls, S., Kim, S.-H., Ladner, R., Marks, K., Nelson, S., Pharaoh, A., Trimmer, R., Rosenberg, J.V., Wallace, G., Weatherall, P., 2009. Global bathymetry and elevation data at 30 arc seconds resolution: SRTM30_PLUS. Mar. Geod. 32 (4), 355–371, URL: http://topex.ucsd.edu/sandwell/publications/124_MG_Becker.pdf.

Bignami, F., Salusti, E., 1990. Tidal currents and transient phenomena in the Strait of Messina: a review. In: Pratt, L. (Ed.), In: The Physical Oceanography of Sea Straits, vol. 318, http://dx.doi.org/10.1007/978-94-009-0677-8_4.

Boyer, T., Antonov, J.I., Baranova, O.K., Coleman, C., Garcia, H.E., Grodsky, A., Johnson, D.R., Locarnini, R.A., Mishonov, A.V., O'Brien, T., Paver, C., Reagan, J., Seidov, D., Smolyar, I.V., Zweng, M.M., 2013. In: Levitus, S., Mishonov, A., Technical Ed. (Eds.), World Ocean Database 2013, NOAA Atlas NESDIS 72. Silver Spring, MD, http://dx.doi.org/10.7289/V5NZ85MT.

Buijsman, M.C., Klymak, J.M., Legg, S., Alford, M.H., Farmer, D., MacKinnon, J.A., Nash, J.D., Park, J.-H., Pickering, A., Simmons, H., 2014. Three-dimensional double-ridge internal tide resonance in Luzon Strait. J. Phys. Oceanogr. 44 (3), 850–869. http://dx.doi.org/10.1175/JPO-D-13-024.1.

Candela, J., Winant, C., Ruiz, A., 1990. Tides in the Strait of Gibraltar. J. Geophys. Res. Ocean. 95 (C5), 7313–7335. http://dx.doi.org/10.1029/JC095iC05p07313.

Carter, G.S., Fringer, O.B., Zaron, E.D., 2012. Regional models of internal tides. Ocean. 25 (2), 56–65, URL: https://www.jstor.org/stable/24861344.

Clementi, E., Aydogdu, A., Goglio, A.C., Pistoia, J., Escudier, R., Drudi, M., Grandi, A., Mariani, A., Lyubartsev, V., Lecci, R., Cretí, S., Coppini, G., Masina, S., Pinardi, N., 2021. Mediterranean Sea physical analysis and forecast (CMEMS MED-Currents, EAS6 system). Copernic. Monit. Environ. Mar. Serv. (CMEMS) http://dx.doi.org/10.25423/CMCC/MEDSEA_ANALYSISFORECAST_PHY_006_013_EAS6.

Copernicus Marine Service, 2024. Global ocean-delayed mode gridded CORA-in-situ observations objective analysis in delayed mode. E.U. Copernic. Mar. Serv. Inf. (CMEMS). Mar. Data Store (MDS) http://dx.doi.org/10.17882/46219.

Coppini, G., Clementi, E., Cossarini, G., Salon, S., Korres, G., Ravdas, M., Lecci, R., Pistoia, J., Goglio, A.C., Drudi, M., Grandi, A., Aydogdu, A., Escudier, R., Cipollone, A., Lyubartsev, V., Mariani, A., Cretì, S., Palermo, F., Scuro, M., Masina, S., Pinardi, N., Navarra, A., Delrosso, D., Teruzzi, A., Di Biagio, V., Bolzon, G., Feudale, L., Coidessa, G., Amadio, C., Brosich, A., Miró, A., Alvarez, E., Lazzari, P., Solidoro, C., Oikonomou, C., Zacharioudaki, A., 2023. The Mediterranean forecasting system. Part I: evolution and performance. EGUsphere 1–50. http://dx.doi.org/10.5194/egusphere-2022-1337.

Cuypers, Y., Bouruet-Aubertot, P., Marec, C., Fuda, J.L., 2012. Characterization of turbulence from a fine-scale parameterization and microstructure measurements in the Mediterranean Sea during the BOUM experiment. Biogeosciences 9 (8), 3131–3149. http://dx.doi.org/10.5194/bg-9-3131-2012.

Deliverable of Perseus, 2012. Deliverable D4.6, SES land-based runoff and nutrient load data (1980–2000), edited by: Bouwman, L. and van Apeldoorn, D.. In: 2012 PERSEUS H2020 Grant Agreement N. 287600, European Commission. URL: http://www.perseus-net.eu/assets/media/PDF/deliverables/33216_Final.pdf.

Demiraj, E., Bicja, M., Gjika, E., Gjiknuri, L., Muçaj, L.G., Hoxha, F., Hoxha, P., Karadumi, S., Kongoli, S., Mullaj, A., Mustaqi, V., Palluqi, A., Ruli, E., Selfo, M., Shehi, A., Sino, Q., 1996. Implications of climate change for the Albanian Coast, Mediterranean Action Plan, MAP Technical Reports Series. (98), UNEP.

Dunphy, M., Lamb, K.G., 2014. Focusing and vertical mode scattering of the first mode internal tide by mesoscale eddy interaction. J. Geophys. Res. Ocean. 119 (1), 523–536. http://dx.doi.org/10.1002/2013JC009293.

Egbert, G.D., Erofeeva, S.Y., 2002. Efficient inverse modeling of barotropic ocean tides. J. Atmosph. Ocean. Tech. 19.2, 183–204.

Egbert, G.D., Ray, R.D., 2003. Semi-diurnal and diurnal tidal dissipation from TOPEX/Poseidon altimetry. Geophys. Res. Lett. 30 (17), 1907. http://dx.doi.org/10.1029/2003GL017676.

Emery, W.J., Lee, W.G., Magaard, L., 1984. Geographic and seasonal distributions of Brunt–Väisälä frequency and Rossby radii in the North Pacific and North Atlantic. J. Phys. Oceanogr. 14, 294–317. http://dx.doi.org/10.1175/1520-0485(1984)014<0294:GASDOB>2.0.CO;2.

Fakete, B., Vörösmarty, C., Grabs, W., 1999. Global Composite Runoff Fields Based on Observed River Discharge and Simulated Water Balances. Technical Report 22, Global Runoff Data Centre, Koblenz, Germany.

Foreman, M.G.G., Cherniawsky, J.Y., Ballantyne, V.A., 2009. Versatile harmonic tidal analysis: Improvements and applications. J. Atmos. Ocean. Technol. 26, 806–817. http://dx.doi.org/10.1175/2008JTECHO615.1.

Galloudec, O.L., Chune, S.L., Nouel, L., Fernandez, E., Derval, C., Tressol, M., Dussurget, R., Biardeau, A., Tonani, M., 2022. Global ocean physical analysis and forecasting product. Copernic. Monit. Environ. Mar. Serv. (CMEMS) http://dx.doi.org/10.48670/moi-00016.

Gaspar, P., Grégoris, Y., Lefevre, J.-M., 1990. A simple eddy kinetic energy model for simulations of the oceanic vertical mixing: Tests at station Papa and long-term upper ocean study site. J. Geophys. Res. Ocean. 95 (C9), 16179–16193. http://dx.doi.org/10.1029/JC095iC09p16179.

Gasparini, G.P., Smeed, D.A., Alderson, S., Sparnocchia, S., Vetrano, A., Mazzola, S., 2004. Tidal and subtidal currents in the Strait of Sicily. J. Geophys. Res. 109, C02011. http://dx.doi.org/10.1029/2003JC002011.

Gates, L.D., Hagemann, S., Golz, C., 1993. Observed historical discharge data from major rivers for climate model validation. Tech. Rep. 307.

GEBCO Bathymetric Compilation Group 2014, 2014. The GEBCO_2014 grid, version 20150318. NERC EDS Br. Ocean. Data Cent. NOC URL: www.gebco.net.

Giorgetta, M.A., Brokopf, R., Crueger, T., Esch, M., Fiedler, S., Helmert, J., Hohenegger, C., Kornblueh, L., Köhler, M., Manzini, E., Mauritsen, T., Nam, C., Raddatz, T., Rast, S., Reinert, D., Sakradzija, M., Schmidt, H., Schneck, R., Schnur, R., Silvers, L., Wan, H., Zängl, G., Stevens, B., 2018. ICON-A, the atmosphere component of the ICON Earth system model: I. model description. J. Adv. Model. Earth Syst. 10 (7), 1613–1637. http://dx.doi.org/10.1029/2017MS001242.

Green, J., Simpson, J., Thorpe, S., Rippeth, T., 2010. Observations of internal tidal waves in the isolated seasonally stratified region of the western Irish Sea. Cont. Shelf Res. 30 (2), 214–225. http://dx.doi.org/10.1016/j.csr.2009.11.004.

Guo, Z., Wang, S., Cao, A., Xie, J., Song, J., Guo, X., 2023. Refraction of the M2 internal tides by mesoscale eddies in the South China Sea. Deep. Sea Res. Part I: Ocean. Res. Pap. 192, 103946. http://dx.doi.org/10.1016/j.dsr.2022.103946.

Hersbach, H., Bell, B., Berrisford, P., Biavati, G., Horányi, A., Muñoz Sabater, J., Nicolas, J., Peubey, C., Radu, R., Rozum, I., Schepers, D., Simmons, A., Soci, C., Dee, D., Thépaut, J.N., 2023. ERA5 hourly data on single levels from 1979 to present (Copernicus Climate Change Service (C3S) Climate Data Store (CDS)). Copernic. Clim. Chang. Serv. (C3S) Clim. Data Store (CDS) http://dx.doi.org/10.24381/cds.adbb2d47.

Kang, D., Fringer, O., 2012. Energetics of barotropic and baroclinic tides in the Monterey Bay area. J. Phys. Oceanogr. 42 (2), 272–290. http://dx.doi.org/10.1175/JPO-D-11-039.1.

Kelly, S.M., Lermusiaux, P.F.J., 2016. Internal-tide interactions with the Gulf Stream and Middle Atlantic Bight shelfbreak front. J. Geophys. Res. Ocean. 121, 6271–6294. http://dx.doi.org/10.1002/2016JC011639.

Korn, P., Brüggemann, N., Jungclaus, J.H., Lorenz, S.J., Gutjahr, O., Haak, H., Linardakis, L., Mehlmann, C., Mikolajewicz, U., Notz, D., Putrasahan, D.A., Singh, V., von Storch, J.S., Zhu, X., Marotzke, J., 2022. ICON-O: The ocean component of the ICON Earth system model—Global simulation characteristics and local telescoping capability. J. Adv. Model. Earth Syst. 14 (10), http://dx.doi.org/10.1029/2021MS002952, e2021MS002952.

Lafuente, J.G., Vargas, J.M., Plaza, F., Sarhan, T., Candela, J., Bascheck, B., 2000. Tide at the eastern section of the Strait of Gibraltar. J. Geophys. Res. Ocean. 105 (C6), 14197–14213. http://dx.doi.org/10.1029/2000JC900007.

Li, Z., von Storch, J.S., 2020. M2 internal-tide generation in STORMTIDE2. J. Geophys. Res. Ocean. 125 (8), http://dx.doi.org/10.1029/2019JC015453, e2019JC015453.

Li, Z., von Storch, J.S., Müller, M., 2015. The M2 internal tide simulated by a 1/10° OGCM. J. Phys. Oceanogr. 45 (12), 3119–3135. http://dx.doi.org/10.1175/JPO-D-14-0228.1.

Li, Z., von Storch, J.S., Müller, M., 2017. The K1 internal tide simulated by a 1/10° OGCM. Ocean. Model. 113, 145–156. http://dx.doi.org/10.1016/j.ocemod.2017.04.002.

Logemann, K., Linardakis, L., Korn, P., Schrum, C., 2021. Global tide simulations with ICON-O: testing the model performance on highly irregular meshes. Ocean. Dyn. 71, 43–57. http://dx.doi.org/10.1007/s10236-020-01428-7.

Lozano, C.J., Candela, J., 1995. The M2 tide in the Mediterranean Sea: Dynamic analysis and data assimilation. Oceanol. Acta 18 (4), 419–441.

Madec, G., Delecluse, P., Imbard, M., Levy, C., 1998. OPA 8.1 ocean general circulation model reference manual. Note Pôle Modélisation 11, URL: https://www.nemo-ocean.eu/wp-content/uploads/Doc_OPA8.1.pdf.

Maderich, V., Ilyin, Y., Lemeshko, E., 2015. Seasonal and interannual variability of the water exchange in the Turkish Straits System estimated by modelling. Mediterr. Mar. Sci. 16 (2), 444–459. http://dx.doi.org/10.12681/mms.1103.

McDonagh, B., 2024. Analysis of the Effects of Barotropic and Internal Tides on the Mediterranean Sea Dynamics Through Numerical Experiments (Ph.D. thesis). University of Bologna.

McDonagh, B., Clementi, E., Goglio, A.C., Pinardi, N., 2024. The characteristics of tides and their effects on the general circulation of the Mediterranean Sea. Ocean. Sci. 20, 1051–1066. http://dx.doi.org/10.5194/os-20-1051-2024.

Merrifield, M.A., Holloway, P.E., Johnston, T.M.S., 2001. The generation of internal tides at the Hawaiian Ridge. Geophys. Res. Lett. 28 (4), 559–562. http://dx.doi.org/10.1029/2000GL011749.

Mihanović, H., Orlić, M., Pasarić, Z., 2009. Diurnal thermocline oscillations driven by tidal flow around an island in the Middle Adriatic. J. Mar. Syst. 78, S157–S168. http://dx.doi.org/10.1016/j.jmarsys.2009.01.021.

Mishonov, A., Boyer, T.P., Baranova, O.K., Bouchard, C.N., Cross, S., Garcia, H.E., Locarnini, R.A., Paver, C.R., Reagan, J.R., Wang, Z., Seidov, D., Grodsky, A.I., Beauchamp, J.G., 2024. In: Bouchard, C., Technical Ed. (Eds.), World Ocean Database 2023: NOAA Atlas NESDIS 97. Silver Spring, MD, http://dx.doi.org/10.25923/z885-h264.

Morozov, E.G., 2018. Oceanic Internal Tides: Observations, Analysis and Modeling: A Global View. Springer, http://dx.doi.org/10.1007/978-3-319-73159-9.

Morozov, E.G., Trulsen, K., Velarde, M.G., Vlasenko, V.I., 2002. Internal tides in the Strait of Gibraltar. J. Phys. Oceanogr. 32 (11), 3193–3206. http://dx.doi.org/10.1175/1520-0485(2002)032<3193:ITITSO>2.0.CO;2.

Müller, M., 2013. On the space- and time-dependence of barotropic-to-baroclinic tidal energy conversion. Ocean. Model. 72, 242–252. http://dx.doi.org/10.1016/j.ocemod.2013.09.007.

Müller, M., Cherniawsky, J.Y., Foreman, M.G.G., von Storch, J.S., 2012. Global M2 internal tide and its seasonal variability from high resolution ocean circulation and tide modeling. Geophys. Res. Lett. 39 (L19607), http://dx.doi.org/10.1029/2012GL053320.

Munk, W., Wunsch, C., 1998. Abyssal recipes II: energetics of tidal and wind mixing. Deep. Sea Res. Part I 45 (12), 1977–2010. http://dx.doi.org/10.1016/S0967-0637(98)00070-3.

Niwa, Y., Hibiya, T., 2001. Numerical study of the spatial distribution of the M2 internal tide in the Pacific Ocean. J. Geophys. Res. Ocean. 106 (C10), 22441–22449. http://dx.doi.org/10.1029/2000JC000770.

Niwa, Y., Hibiya, T., 2014. Generation of baroclinic tide energy in a global three-dimensional numerical model with different spatial grid resolutions. Ocean. Model. 80, 59–73. http://dx.doi.org/10.1016/j.ocemod.2014.05.003.

Oddo, P., Poulain, P., Falchetti, S., Storto, A., Zappa, G., 2023. Internal tides in the central Mediterranean Sea: observational evidence and numerical studies. Ocean. Dyn. 73, 145–163. http://dx.doi.org/10.1007/s10236-023-01545-z.

Pettenuzzo, D., Large, W., Pinardi, N., 2010. On the corrections of ERA-40 surface flux products consistent with the Mediterranean heat and water budgets and the connection between basin surface total heat flux and NAO. J. Geophys. Res. 115 (C06022), http://dx.doi.org/10.1029/2009JC005631.

Raicich, F., 1996. On the fresh balance of the Adriatic Sea. J. Mar. Syst. 9 (3), 305–319. http://dx.doi.org/10.1016/S0924-7963(96)00042-5.

Ray, R.D., Zaron, E.D., 2016. M2 internal tides and their observed wavenumber spectra from satellite altimetry. J. Phys. Oceanogr. 46 (1), 3–22. http://dx.doi.org/10.1175/JPO-D-15-0065.1.

Röske, F., 2006. A global heat and freshwater forcing dataset for ocean models. Ocean. Model. 11 (3), 235–297. http://dx.doi.org/10.1016/j.ocemod.2004.12.005.

Sannino, G., Herrmann, M., Carillo, A., Rupolo, V., Ruggiero, V., Artale, V., Heimbach, P., 2009. An eddy-permitting model of the Mediterranean Sea with a two-way grid refinement at the Strait of Gibraltar. Ocean. Model. 30 (1), 56–72. http://dx.doi.org/10.1016/j.ocemod.2009.06.002.

Schwab, D.J., Rao, D.B., 1983. Barotropic oscillations of the Mediterranean and Adriatic Seas. Tellus A 35A (5), 417–427. http://dx.doi.org/10.1111/j.1600-0870.1983.tb00216.x.

Shriver, J.F., Arbic, B.K., Richman, J.G., Ray, R.D., Metzger, E.J., Wallcraft, A.J., Timko, P.G., 2012. An evaluation of the barotropic and internal tides in a high-resolution global ocean circulation model. J. Geophys. Res. 117 (C10024), http://dx.doi.org/10.1029/2012JC008170.

St. Laurent, L.C., Simmons, H.L., Jayne, S.R., 2002. Estimating tidally driven mixing in the deep ocean. Geophys. Res. Lett. 29 (2106), http://dx.doi.org/10.1029/2002GL015633.

Tsimplis, M.N., Proctor, R., Flathe, R.A., 1995. A two-dimensional tidal model for the Mediterranean Sea. J. Geophys. Res. 100 (C8), 16223–16239. http://dx.doi.org/10.1029/95JC01671.

von Storch, J.S., Hertwig, E., Lüschow, V., Brüggemann, N., Haak, H., Korn, P., Singh, V., 2023. Open-ocean tides simulated by ICON-O, version icon-2.6.6. Geosci. Model. Dev. 16, 5179–5196. http://dx.doi.org/10.5194/gmd-16-5179-2023.

Wunsch, C., 1975. Internal tides in the ocean. Rev. Geophys. Space Phys. 13 (1), 167–182. http://dx.doi.org/10.1029/rg013i001p00167.